MOX-Report No. 28/2015

Beading instability in soft cylindrical gels with capillary energy: weakly non-linear analysis and numerical simulations

Taffetani, M.; Ciarletta, P.

MOX, Dipartimento di Matematica
Politecnico di Milano, Via Bonardi 9 - 20133 Milano (Italy)

mox-dmat@polimi.it http://mox.polimi.it

Beading instability in soft cylindrical gels with capillary energy: weakly non-linear analysis and numerical simulations

Matteo Taffetani[1] Pasquale Ciarletta[2]

June 10, 2015

[1] MOX, Dipartimento di Matematica, Politecnico di Milano Fondazione CEN
Piazza Leonardo da Vinci 32, I-20133 Milano, Italy
E-mail: matteo.taffetani@polimi.it

[2] MOX, Dipartimento di Matematica, Politecnico di Milano Fondazione CEN
Piazza Leonardo da Vinci 32, I-20133 Milano, Italy
CNRS and Institut Jean le Rond d'Alembert, UMR 7190, Université Paris 6
4 place Jussieu case 162, 75005 Paris, France
E-mail: pasquale.ciarletta@upmc.fr

Abstract

Soft cylindrical gels can develop a long-wavelength peristaltic pattern driven by a competition between surface tension and bulk elastic energy. In contrast to the Rayleigh-Plateau instability for viscous fluids, the macroscopic shape in soft solids evolves toward a stable beading, which strongly differs from the buckling arising in compressed elastic cylinders.
This work proposes a novel theoretical and numerical approach for studying the onset and the non-linear development of the elasto-capillary beading in soft cylinders, made of neo-Hookean hyperelastic material with capillary energy at the free surface, subjected to axial stretch. Both a theoretical study, deriving the linear and the weakly non-linear stability analyses for the problem, and numerical simulations, investigating the fully non-linear evolution of the beaded morphology, are performed. The theoretical results prove that an axial elongation can not only favour the onset of beading, but also determine the nature of the elastic bifurcation. The fully non-linear phase diagrams of the beading are also derived from finite element numerical simulations, showing two peculiar morphological transitions when varying either the axial stretch or the material properties of the gel. Since the bifurcation is found to be subcritical for very slender cylinders, an imperfection sensitivity analysis is finally performed. In this case, it is shown that a surface sinusoidal imperfection can resonate with the corresponding marginally stable solution, thus selecting the emerging beading wavelength.
In conclusion, the results of this study provide novel guidelines for controlling the beaded morphology in different experimental conditions, with important applications in micro-fabrication techniques, such as electrospun fibres.

1 Introduction

Shape instability in elastic materials has historically been a subject of great interest in applied mechanics. Early works focused on determining the stability conditions for avoiding the

loss of structural integrity and functionality, e.g. in shell structure [33]. Conversely, a more recent idea is to control the conditions triggering the onset of the instability and the pattern evolution for guiding applications in many fields [29], such as developing tunable pattern [44], improving the efficiency of electronic devices [13, 28] or understanding the shape emergence in biological systems [37].

As pointed out in the review proposed by Li et al. [30], three main classes of instability mechanisms can be identified: wrinkling, folding and creasing (also referred to as sulcification). Since the pioneering work of Biot [5] on the wrinkling of an incompressible elastic half-space, it has been shown that a compressive strain may trigger a bifurcation in systems which are uniquely governed by bulk elasticity. More recently, Cao and Hutchinson [10] evaluated the wrinkling to creasing transition in compressed elastomers, whilst the nature of sulcification in a compressed elastic half-space has been investigated by Hohlfeld and Mahadevan [25] and Tallinen et al. [46], also introducing numerical tools. Theoretical and numerical analysis of the wrinkling onset and post-buckling evolution in film-substrate systems under compression has been proposed by Cao and Hutchinson [9] and Hutchinson [26] for a wide range of material properties. The formation of stable folds in compressed thin films over soft substrates has been, instead, investigated by Brau et al. [7]. In layered materials, the competition of the bulk energies has been also found to determine pattern selection and dynamics in many biological systems, from solid tumours [15] to tubular tissues [19], in dependence of both size and elastic effects.

When a superficial energy is considered, its competition with the bulk energy has been found to trigger morphological transitions both under compression and elongation. This phenomenon is well known in fluid mechanics since the experimental work of Savart [42] and the theoretical analysis of Reyleigh [40]: the Rayleigh-Plateau instability (RPI) describes how a viscous fluid jet can undergo a varicose shape transition driven by the competition between the surface tension and the fluid inertia. Regarding viscous fluids, the capillary instabilities are still widely studied for their importance in guiding fabrication techniques [41], such as the use of droplet impact to select patterns in folded solid structures [2].
Competition between bulk and superficial energies in solids can be found in the case of the Asaro-Tiller-Grinfeld instability [3, 23], a typical example of how the combination of the superficial tension and the accumulation of the elastic stresses makes a folded structure energetically more favourable during the deposition process of an elastic solid on a substrate, and in case of soft layers under equal bi-axial compressive strain, where the emergence of different surface patterns has been proved by means of a weakly non-linear analysis [16].
Focusing on the particular case of soft elastic cylinders with a superficial energy, Barriere et al. [4] proved that capillarity may drive the onset of a long-wavelength peristaltic pattern without the application of any external strain, differently from the short-wavelength buckling arising in compressed cylinders with negligible surface effects [47]. More recently, Mora et al. [35] proposed a linear stability analysis for this elastocapillary problem, validating their theoretical predictions with experiments made on soft gel fibres. It has been proved that a typical length L_{ec}, defined as the ratio between the surface tension and the shear modulus of the material, controls the peristaltic instability, competing with the characteristic dimension of the body: therefore, the miniaturization of the elastic system is intuitively found to favour the onset of a shape instability. Recent experiments have also shown that, when L_{ec} is of the same order of the characteristic dimension, a fibre elongation can even favour the onset

of this instability, as seen in soft elastic gels [34], electrospun fibres [21, 36], stretched nerves [37] and mitochondria [27].
Despite this large availability of experimental evidences, there still lacks a comprehensive mathematical analysis describing the interplay between the geometry, the applied stretch and the material properties for driving pattern formation, especially far beyond the linear stability threshold. The aim of this work is to provide a theoretical foundation of beading instability, through both linear and weakly non-linear stability analysis, and to perform a numerical investigation of its fully non-linear behaviour. The cylinder is assumed to behave as a neo-Hookean incompressible hyperelastic material with a capillary energy at the free surface. In fact, soft gels as the ones investigated in Matsuo and Tanaka [34] and Mora et al. [35], are mostly composed by water immersed in a cross-linked polymeric network, which allow absorbing even larger quantities of water without dissolving. Accordingly, soft gels can undergo drastic volume changes in response to solvent concentration, showing a solid elastic behaviour with fluid-like surface tension at the free surface [43].

The paper is organized as follow. In Section 2, we introduce the elastocapillary model and we derive a variational formulation using a suitable generating function for the axisymmetric problem. The linear stability analysis is performed in Section 3 whilst the weakly non-linear study is derived in Section 4. Two different experimental conditions are investigated: (i) the elastocapillary ratio L_{ec} is kept fixed whilst the fibre is elongated; (ii) the elastocapillary ratio is changed at constant stretch. The derivation of amplitude equations for the peristaltic pattern is given in Section 5. The numerical model, described in Section 6, is used to analyse the fully non-linear regime, after being validated against the theoretical results. An imperfection sensitivity analysis is performed in Section 7, whilst the main results of this work are summarized and discussed in Section 8, together with some concluding remarks.

2 Elastocapillary model

In this Section we present the theoretical model of the elastocapillary problem under analysis. First, we introduce the kinematics and constitutive assumptions. Second, we propose a variational formulation of the axisymmetric problem using a non-linear stream function. Finally, we derive the Euler-Lagrange equations of the problem and the basic axisymmetric solution.

2.1 Kinematic and constitutive assumptions

Let us consider a solid cylinder of undeformed outer radius R_0 and undeformed length L_0. In cylindrical coordinates, the set $[R, \Theta, Z]$ defines the polar coordinates in the material configuration, whilst the set $[r, \theta, z]$ refers to spatial configuration. The cylinder has volume Ω_0 and boundary $\Gamma_0 := (R = R_0)$ in its undeformed configuration; so that a generic point $\mathcal{P} \in \Omega_0$ is described by the material position vector $\mathbf{X}$. The mapping χ biunivocally identifies the spatial position $\mathbf{x} = \chi(\mathbf{X})$ in the deformed configuration, in which the cylinder has a volume Ω and a boundary Γ. Accordingly, the deformation gradient tensor $\mathbf{F}$ can be defined as

$$\mathbf{F} = Grad(\chi) \tag{1}$$

where *Grad* indicates the material gradient operator; the right and left Cauchy-Green tensors $\mathbf{C}$ and $\mathbf{B}$ read

$$\mathbf{C} = \mathbf{F^T F}; \quad \mathbf{B} = \mathbf{F F^T} \tag{2}$$

The cylinder is made of a soft gel, which can be modelled by a bulk elastic energy associated with a capillary energy at the free surface. Thus, its total potential energy Π can be decomposed into an elastic contribution Ψ_e and a superficial term Ψ_s

$$\Pi = \Psi_e + \Psi_s \tag{3}$$

where the presence of body forces is neglected. The cylinder is assumed to behave as an incompressible neo-Hookean hyperelastic material of strain energy density Ψ, so that the elastic energy Ψ_e can be written as

$$\Psi_e = \int_{\Omega_0} \Psi d\Omega_0 = \int_{\Omega} \Psi \frac{1}{J} d\Omega = \int_{\Omega_0} \left[\frac{\mu}{2} (I_1 - 3) - p (J - 1) \right] d\Omega_0 \tag{4}$$

where μ is the shear modulus, $J = \det F$ is the Jacobian of the transformation, $I_1 = tr(C)$ is the first invariant of $\mathbf{C}$ and p is the Lagrangian multiplier enforcing the incompressibility constraint. Due to the incompressibility assumption, $J = 1$ has been imposed in the following equations.
Being $\mathbf{N}$ and $\mathbf{n}$ the unit normal vectors to the external surface in reference of spatial configurations, the Nanson's formula states that $\mathbf{n} d\Gamma = \mathbf{F^{-T}} \mathbf{N} d\Gamma_0$. Accordingly, the superficial contribution to the potential energy can be written as

$$\Psi_s = \int_{\Gamma} \gamma d\Gamma = \int_{\Gamma_0} \frac{\gamma}{\|\mathbf{F^{-T}} \mathbf{N}\|} d\Gamma_0 \tag{5}$$

where γ is the surface tension of the soft solid with the environment.
Being ρ_0 the density of the material, the kinetic energy K can be expressed as:

$$K = \frac{1}{2} \int_{\Omega_0} \rho_0 \mathbf{v_s}^2 d\Omega_0 = \frac{1}{2} \int_{\Omega} \rho_0 \mathbf{v_s}^2 d\Omega \tag{6}$$

where $\mathbf{v}_s$ is the spatial velocity vector. The elastic stress measures in the material and spatial configurations are given through the first Piola-Kirchhoff stress tensor $\mathbf{P}$ and the Cauchy stress tensor $\boldsymbol{\sigma}$, respectively, which read:

$$\begin{aligned} \mathbf{P} = \frac{\partial \Psi_e}{\partial \mathbf{F}} &= \left(\mu \mathbf{F}^T - p \mathbf{F}^{-1} \right) \\ \boldsymbol{\sigma} &= \mathbf{F P} = \mu \mathbf{B} - p \mathbf{I} \end{aligned} \tag{7}$$

Thus, the equilibrium equations in reference and spatial configurations can be written as:

$$\begin{aligned} \rho_0 \dot{\mathbf{v}}_\mathbf{s} &= Div \mathbf{P} \quad in\ \Omega_0 \\ \rho_0 \dot{\mathbf{v}}_\mathbf{s} &= div \boldsymbol{\sigma} \quad in\ \Omega \end{aligned} \tag{8}$$

where *Div* and *div* are the material and spatial divergence operators, respectively. Moreover, the boundary conditions at the free surface read:

$$\begin{aligned} \mathbf{N} \cdot \mathbf{P} &= \gamma C_0 \mathbf{N} \quad in\ \Gamma_0 \\ \mathbf{n} \cdot \boldsymbol{\sigma} &= \gamma C \mathbf{n} \quad in\ \Gamma \end{aligned} \tag{9}$$

where $C_0 = tr(\mathbf{K}_0)$ and $C = tr(\mathbf{K})$ are the traces of the material and spatial curvature tensors at free surface, $\mathbf{K}_0$ and $\mathbf{K}$, respectively.

Let the cylinder be subjected to an axial strain λ_z; then, in a cylindrical reference system, the homogeneous, axisymmetric solution of the elastocapillary problem is given by:

$$r = \frac{R}{\sqrt{\lambda_z}}, \quad z = \lambda_z Z \quad \text{and} \quad \theta = \Theta \tag{10}$$

so that the deformation gradient tensor rewrites:

$$\mathbf{F} = \frac{1}{\sqrt{\lambda_z}}\mathbf{e}_r \otimes \mathbf{E}_R + \frac{1}{\sqrt{\lambda_z}}\mathbf{e}_\theta \otimes \mathbf{E}_\Theta + \lambda_z \mathbf{e}_z \otimes \mathbf{E}_Z \tag{11}$$

where the orthonormal bases in the reference cylindrical configuration, $[\mathbf{E}_R, \mathbf{E}_\Theta, \mathbf{E}_Z]$, and in the current cylindrical configuration, $[\mathbf{e}_r, \mathbf{e}_\theta, \mathbf{e}_z]$, are introduced. The corresponding value p_0 of the Lagrange multiplier is given by the boundary conditions in Equation (9):

$$p_0 = \frac{\mu}{\lambda_z} + \frac{\gamma}{r_0} \tag{12}$$

with $r_0 = \frac{R_0}{\lambda_z}$ being the deformed outer radius of the stretched cylinder.
The stability of the axisymmetric solution can be studied applying an infinitesimal displacement over the basic finite deformation [38], deriving the incremental elastic problem through series expansion of the equilibrium equations in Equation (8) with boundary conditions in Equations (9). Using this approach, the incremental boundary value problem can be written as a function of four scalar functions, being the three components of the incremental displacement and the relative perturbation of the Lagrangian multiplier p around the homogeneous state described by the Equations (11) and (12).
Another approach will be used in this paper: the linear stability analysis will be performed by perturbing only one scalar field, representing the generating function of an incompressible axisymmetric mapping [17, 18]. Accordingly, we derive a variational formulation that does not require the introduction of a Lagrangian multiplier, since the incompressibility constraint is exactly fulfilled by a stream function which is the elastic equivalent of the one used for incompressible two-dimensional viscous flows. This will allow a more straightforward derivation of the weakly non-linear analysis. We remark that the generating function has been first proposed by Carroll [11], while the isochoric transformation considered in this work is adapted from Ciarletta [14].

2.2 Definition of a stream function for axisymmetric deformations

As proposed by Ciarletta [14], we identify an intermediate configuration of volume $\overline{\Omega}$ and boundary $\overline{\Gamma}$ in the set of mixed coordinates $[R, \Theta, z]$, where the orthonormal triad is constituted by the mixed unit vectors $[\mathbf{E_R}, \mathbf{E_\Theta}, \mathbf{e_z}]$. For sake of simplicity, in the following, we drop the angular coordinate since an axisymmetric problem is considered. A stream function $\phi(R, z)$ enforcing the incompressibility constraint can be written as

$$r^2 = 2\phi_{,z} \quad \text{and} \quad Z = \frac{1}{R}\phi_{,R} \tag{13}$$

where comma denotes partial derivative. Therefore, the deformation gradient tensor $\mathbf{F}$ rewrites in terms of the stream function as:

$$\mathbf{F} = \begin{bmatrix} \frac{\phi_{,Rz}}{\sqrt{2\phi_{,z}}} - \frac{\phi_{,zz}\left(\phi_{,RR} - \frac{\phi_{,R}}{R}\right)}{\sqrt{2\phi_{,z}}\phi_{,Rz}} & \frac{\phi_{,zz}R}{\phi_{,Rz}\sqrt{2\phi_{,z}}} & 0 \\ \frac{\phi_{,R}}{\phi_{,Rz}R} - \frac{\phi_{,RR}}{\phi_{,Rz}} & \frac{R}{\phi_{,Rz}} & 0 \\ 0 & 0 & \frac{\sqrt{2}\sqrt{\phi_{,z}}}{R} \end{bmatrix} \tag{14}$$

It can be easily checked that $\det \mathbf{F} = 1$ is automatically satisfied.

2.3 Variational formulation and Euler-Lagrange equations

Accordingly, the elastic energy Ψ_e, the superficial energy Ψ_s and the kinetic energy K rewrite in terms of the stream function in Equation (13) as:

$$\begin{aligned} \Psi_e = \int_{\overline{\Omega}} \overline{\Psi_e} d\overline{\Omega} = 2\pi \int_0^{R_0} \int_0^{L_0\lambda_z} \frac{1}{2}\mu \Bigg(& \frac{1}{2\phi_{,z}} \left(\phi_{,Rz} - \frac{\phi_{,zz}\left(\phi_{,RR} - \frac{\phi_{,R}}{R}\right)}{\phi_{,Rz}} \right)^2 \\ & + \left(\frac{\phi_{,R}}{\phi_{,Rz}R} - \frac{\phi_{,RR}}{\phi_{,Rz}} \right)^2 + \frac{\phi_{,zz}^2 R^2}{2\phi_{,Rz}^2\phi_{,z}} + \frac{R^2}{\phi_{,Rz}^2} + \frac{2\phi_{,z}}{R^2} - 3 \Bigg) \phi_{,Rz} dR dz \end{aligned} \tag{15}$$

$$\Psi_s = \int_{\overline{\Gamma}} \overline{\Psi_s} d\overline{\Gamma} = 2\pi\gamma \int_0^{L_0\lambda_z} \left(\sqrt{2\phi_{,z} + \phi_{,zz}^2} \right) dz \tag{16}$$

$$K = \int_{\overline{\Omega}} \overline{K} d\overline{\Omega} = 2\pi \int_0^{R_0} \int_0^{L_0\lambda_z} \frac{1}{2}\rho_0 \left(\frac{\phi_{,Rt}^2}{\phi_{,Rz}^2} + \left(\frac{\phi_{,zt}}{\sqrt{2}\sqrt{\phi_{,z}}} - \frac{\phi_{,Rt}\phi_{,zz}}{\sqrt{2}\phi_{,Rz}\sqrt{\phi_{,z}}} \right)^2 \right) \phi_{,Rz} dR dz \tag{17}$$

The Lagrangian functional L can, than, be written as

$$L\left(\phi_R, \phi_z, \phi_{,RR}, \phi_{,zz}, \phi_{,Rz}\right) = K - \Pi \tag{18}$$

Using a variational approach, the equilibrium is derived by imposing the minimization of the Lagrangian L, that means $\delta L = 0$ with respect to any variation of the stream function. After integration by parts, the corresponding bulk Euler-Lagrange equation reads:

$$\left(\frac{\partial\overline{\Psi_e}}{\partial\phi_{,RR}}\right)_{,RR} + \left(\frac{\partial\overline{\Psi_e}}{\partial\phi_{,Rz}}\right)_{,Rz} - \left(\frac{\partial\overline{K}}{\partial\phi_{,Rt}}\right)_{,Rt} + \left(\frac{\partial\overline{\Psi_e}}{\partial\phi_{,zz}}\right)_{,zz} - \left(\frac{\partial\overline{K}}{\partial\phi_{,zt}}\right)_{,zt} - \left(\frac{\partial\overline{\Psi_e}}{\partial\phi_{,R}}\right)_{,R} - \left(\frac{\partial\overline{\Psi_e}}{\partial\phi_{,z}}\right)_{,z} = 0 \tag{19}$$

The fourth order partial differential Equation (19) requires four boundary conditions. Two of them are given by imposing the regularity of the solution at $R = 0$; the other two arise from the surface Euler-Lagrange equations to arbitrary variations on ϕ and $\phi_{,R}$ at the outer radius, respectively:

$$\frac{\partial\overline{\Psi_e}}{\partial\phi_{,R}} - \left(\frac{\partial\overline{\Psi_e}}{\partial\phi_{,RR}}\right)_{,R} - \left(\frac{\partial\overline{\Psi_e}}{\partial\phi_{,Rz}}\right)_{,z} + \left(\frac{\partial\overline{\Psi_s}}{\partial\phi_{,zz}}\right)_{,zz} - \left(\frac{\partial\overline{\Psi_s}}{\partial\phi_{,z}}\right)_{,z} = 0 \quad at \quad R = R_0 \tag{20}$$

$$\frac{\partial \overline{\Psi_e}}{\partial \phi_{,RR}} = 0 \quad at \quad R = R_0 \tag{21}$$

Within the proposed variational framework, the stability analysis will be performed by considering a perturbation on $\phi(R,z)$, so that incremental boundary value problem will be derived by performing a series expansion of Equation (19) with the boundary conditions in Equations (20) and (21).

3 Linear stability analysis

In terms of the basic stream function $\phi_0(R,z)$, the homogeneous solution in Equation (10) can be rewritten as

$$\phi_0(R,z) = \frac{R^2\ z}{2\lambda_z} \tag{22}$$

Let us now consider an infinitesimal periodic perturbation $\phi_1(R,z,t)$ around the homogeneous condition. Setting $|\epsilon| \ll 1$, the solution at the first order using variables separation reads:

$$\phi(R,z,t) = \phi_0(R,z) + \epsilon\phi_1(R,z,t) = \phi_0(R,z) + \epsilon R u\left(\frac{R}{\sqrt{\lambda_z}}\right) e^{\mathbb{I}k(z-Vt)} + c.c. \tag{23}$$

where V is the axial velocity of the travelling wave, e identifies the exponential function, $\mathbb{I}$ denotes the imaginary unit, $k = \frac{2\pi n_f}{L_0}$ defines the axial perturbation mode, with n_f a positive integer number, $u\left(\frac{R}{\sqrt{\lambda_z}}\right)$ is an unknown scalar function and *c.c.* indicates the complex conjugate.

For sake of clarity, we set in the following $r = R/\sqrt{\lambda_z}$ so that $u\left(\frac{R}{\sqrt{\lambda_z}}\right) = u(r) = u$. Substituting Equation (23) in Equation (19), the bulk Euler-Lagrange equation at the first order in ϵ rewrites

$$\mathcal{L}_{1,1}\left[\mathcal{L}_{q,1}(u)\right] = 0 \tag{24}$$

where:

$$\mathcal{L}_{f,j} = \left(\frac{\partial^2}{\partial r^2}\right) + \frac{1}{r}\frac{\partial}{\partial r} - \frac{1}{r^2} - f^2 j^2 k^2 \tag{25}$$

for $j \in \mathbb{N}^+$ and $f = (1,q)$. The parameter q is defined as

$$q = \sqrt{\lambda_z\left(\lambda_z^2 - \frac{V^2}{c^2}\right)} \tag{26}$$

with $c = \sqrt{\mu/\rho_0}$ being the speed of sound inside the material. The first boundary condition can be obtained from Equation (20) as

$$\mathcal{L}_{1,1}(u) + 2k^2 u = 0 \quad at \quad r = r_0 = \frac{R_0}{\sqrt{\lambda_z}} \tag{27}$$

whereas the second boundary condition from Equation (21) reads

$$\begin{aligned} &\Big(r\left(\left(2k^2r^2+1\right)u' + r\left(-ru''' - 2u''\right)\right) - u \\ &+k^2r^2\left(ru'+u\right)q^2 + \frac{\gamma}{\mu}k^2\lambda_z ru\left(1-k^2r^2\right)\Big) = 0 \quad at \quad r = r_0 = \frac{R_0}{\sqrt{\lambda_z}} \end{aligned} \tag{28}$$

The solution of Equation (24) with boundary conditions in Equations (27) and (28) depends on parameter q. In the following, we will focus on two different situations: (i) $q \neq 1$; (ii) $q = 1$. For sake of clarity, let us also introduce two dimensionless quantities: (i) $\bar{k} = kR_0$, representing the dimensionless wavenumber; and (ii) the elastocapillary ratio $\frac{L_{ec}}{R_0} = \frac{\gamma}{(\mu R_0)}$, representing the ratio between the elastocapillary length $L_{ec} = \frac{\gamma}{\mu}$ and the undeformed radius R_0 of the cylinder.

3.1 Linear stability analysis for $q \neq 1$

If $q \neq 1$, Equation (24) admits the modified Bessel functions of first order I_1 and K_1 as eigensolutions [48]. Imposing the regularity of the solution at $r = 0$, the solution of Equation (24) rewrites

$$u = \frac{I_1(krq)}{I_1(kr_0q)} + \beta \frac{I_1(kr)}{I_1(kr_0)} \tag{29}$$

The coefficient β can be derived from Equations (27) and (29) as:

$$\beta = -\frac{q^2+1}{2} \tag{30}$$

The dispersion relation can be obtained from Equation (28) by inserting the solution in Equation (29) and the value of β as in Equation (30). In terms of dimensionless quantities, the dispersion relation becomes:

$$\lambda_z\left(q^2-1\right)\left(\frac{L_{ec}}{R_0}\sqrt{\lambda_z}\left(\lambda_z-\bar{k}^2\right)-\frac{2}{\sqrt{\lambda_z}}\right)+\bar{k}\left(-\frac{\left(q^2+1\right)^2 I_0\left(\frac{\bar{k}}{\sqrt{\lambda_z}}\right)}{I_1\left(\frac{\bar{k}}{\sqrt{\lambda_z}}\right)}+\frac{4qI_0\left(\frac{\bar{k}q}{\sqrt{\lambda_z}}\right)}{I_1\left(\frac{\bar{k}q}{\sqrt{\lambda_z}}\right)}\right)=0 \tag{31}$$

It can be shown from Equation (31), that the marginal stability curve with the minimum applied stretch λ_z corresponds to the stationary condition $V = 0$, so that $q = \lambda_z^{3/2}$. Accordingly, the dispersion relation simplifies as:

$$2\sqrt{\lambda_z}\left(\lambda_z^3-1\right)+\bar{k}\left[4\lambda_z^{\frac{3}{2}}\frac{I_0\left(\bar{k}\lambda_z\right)}{I_1\left(\bar{k}\lambda_z\right)}-\left(\lambda_z^3+1\right)^2\frac{I_0\left(\frac{\bar{k}}{\sqrt{\lambda_z}}\right)}{I_1\left(\frac{\bar{k}}{\sqrt{\lambda_z}}\right)}\right]+\frac{L_{ec}}{R_0}\lambda_z^2\left(\lambda_z^3-1\right)\left(1-\frac{\bar{k}^2}{\lambda_z}\right)=0 \tag{32}$$

This relation shows that the occurrence of a beading instability is driven by both the applied stretch λ_z and the elastocapillary ratio $\frac{L_{ec}}{R_0}$, as shown in Figure 1. In fact, if we let $\bar{k}$ be the independent variable, the marginal stability threshold are depicted in terms of either $\left(\frac{L_{ec}}{R_0}\right)^{th}$, when different λ_z are applied (see Figure 1(a), all lines except the black one), or λ_z^{th} at fixed values of $\frac{L_{ec}}{R_0}$ (see Figure 1(b)). In particular, it is found that, in all the cases, the instability first occurs at long wavelength, i.e. for $\bar{k} \to 0$, and, within this limit, the condition for beading instability onset reduces to:

$$\gamma = 2\mu R_0 \frac{\left(\lambda_z^3+2\right)}{\lambda_z^{\frac{3}{2}}} \tag{33}$$

The application of an axial elongation favours the onset of beading. Indeed, Equation (33) allows also to estimate a lower limit of $L_{ec}/R_0 = 4\sqrt{2} \approx 5.65$ under which no instability can occurs whatever is the stretch applied: at that point, the limit stretch is $\lambda_z^{th} = 2^{1/3} \approx 1.26$.

3.2 Linear stability analysis for $q = 1$

When $q = 1$, the solution of Equation (24) can be found by applying the Wronskian method. Imposing the regularity at $r = 0$, the solution can be written as

$$u = I_1(kr) + \beta \left[K_1(kr) \int_0^r r I_1^2(kr)\, dr - I_1(kr) \int_0^r r I_1(kr) K_1(kr)\, dr \right] \tag{34}$$

In this case, coefficient β is derived from Equation(27) with Equation (34), being:

$$\beta = -\frac{\left(4\sqrt{\pi} k^2 I_1(kr)\right)}{D_\beta} \tag{35}$$

with

$$D_\beta = 2\sqrt{\pi} kr_0 \left(\left(-kr_0 I_0(kr_0)^2 + I_1(kr_0) I_0(kr_0) + kr_0 I_1(kr_0)^2 \right) K_1(kr_0) - I_1(kr_0)^2 K_0(kr_0) \right) - I_1(kr_0) MG \tag{36}$$

and MG describing the Maijer G-function $G_{2,4}^{2,2}\left(k^2 r_0^2 \middle| \begin{matrix} 1, \frac{3}{2} \\ 1, 2, 0, 0 \end{matrix} \right)$ [1].

The corresponding dispersion relation is obtained from Equation (28), substituting Equations (34) and (35), being:

$$2\mu R_0 I_0\left(\frac{\bar{k}}{\sqrt{\lambda_z}}\right)^2 - \frac{1}{\bar{k}^2} I_1\left(\frac{\bar{k}}{\sqrt{\lambda_z}}\right)^2 \left(\gamma \lambda_z^{3/2} \left(\lambda_z - \bar{k}^2\right) + 2\mu R_0 \left(\bar{k}^2 + \lambda_z\right) \right) = 0 \tag{37}$$

The dispersion relation confirms that the instability first occurs at long wavelengths. Taking the limit for $\bar{k} \to 0$, it becomes:

$$\frac{6R_0}{L_{ec}} - \lambda_z^{\frac{3}{2}} = 0 \tag{38}$$

The condition $q = 1$ implies $\lambda_z = \frac{\left(V^2 + \sqrt{V^4 + 4c^4}\right)}{(2c^2)}$, so that $\lambda_z \geq 1$. The first marginally unstable elastocapillary ratio $\left(\frac{L_{ec}}{R_0}\right)^{th}$ from Equation (38) corresponds to $\lambda_z = 1$, which implies the stationary condition $V = 0$. From Equation (37), the simplified dispersion relation rewrites:

$$2I_0(\bar{k})^2 + \frac{1}{\bar{k}^2} \left(\frac{L_{ec}}{R_0} \left(\bar{k}^2 - 1\right) - 2\left(\bar{k}^2 + 1\right) \right) I_1(\bar{k})^2 = 0 \tag{39}$$

The plot of this function is presented in Figure 1(a) (black curve). The threshold condition $L_{ec} = 6R_0$, found in Barriere et al. [4] using linear elasticity, is recovered in our analysis both imposing $\lambda_z = 1$ in Equation (33) or computing the limit for $\bar{k} \to 0$ of Equation (39). It is worth mentioning that the results provided in this subsection are slightly different from the ones proposed by Mora et al. [35] since we require our solution to be regular at $r = 0$ as shown in Equation (34).

4 Weakly non-linear stability analysis

The two different conditions on the parameter q that have been discussed during the linear stability analysis are related to two particular experimental situations. The condition $q \neq 1$

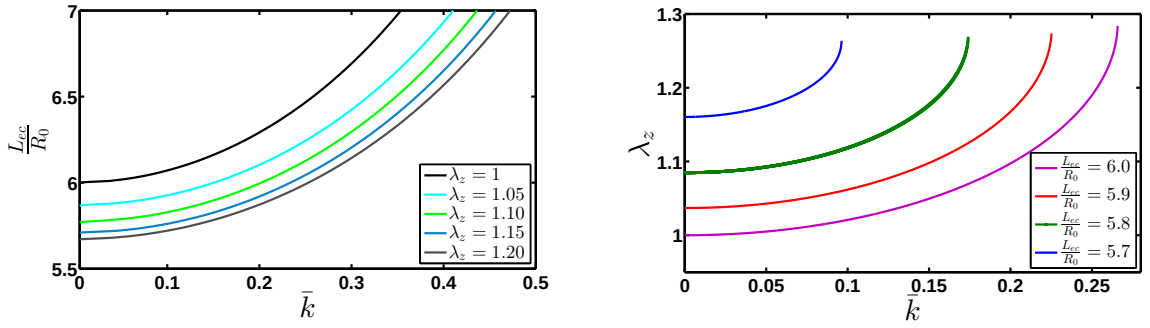

(a) (b)

Figure 1: Linear stability thresholds versus the dimensionless wavenumber $\bar{k}$ for (a) the elastocapillary ratio $\frac{L_{ec}}{R_0}$, at different stretched λ_z, and (b) the applied stretch λ_z, at different elastocapillary ratios $\frac{L_{ec}}{R_0}$. The case $q = 1$ in our study is represented by the black line in (a).

corresponds to the case of a cylinder stretched of an amount λ_z when the elastocapillary ratio is kept fixed [21, 37, 36]: in the following, it will be denoted as Case (1). Condition $q = 1$, instead, corresponds to the case of an unstretched cylinder, $\lambda_z = 1$, when its elastocapillary ratio is varied [35]: in the following, it will be denoted as Case (2). The experimental counterparts of the mathematical assumption are necessary to define the control parameters of the beading instability to be used in the following weakly non-linear analysis. The control parameters will be the axial stretch λ_z in Case (1) and the shear modulus μ in Case (2). Indeed, assuming constant values for γ and R_0 in the latter case, μ^{th} is uniquely determined from $\left(\frac{L_{ec}}{R_0}\right)^{th}$.

The purpose of this Section is to investigate the weakly non-linear evolution of the perturbation amplitude of the linearly unstable waves in the vicinity of the marginal stability threshold. The order parameter ϵ for the two cases under analysis are given by:

$$\begin{cases} \epsilon = \sqrt{\frac{\lambda_z - \lambda_z^{th}}{\lambda_z^{th}}} & if \;\; \mathbf{Case(1)} : \frac{L_{ec}}{R_0} = \text{constant} \\ \epsilon = \sqrt{\frac{\mu^{th} - \mu}{\mu^{th}}} & if \;\; \mathbf{Case(2)} : \lambda_z = 1 \end{cases} \tag{40}$$

A multiple-scale approach will be used in the following to perform the weakly non-linear analysis. Assuming a small deviation from the linear threshold in Equation (40), the velocity V of the near-critical travelling wave can be estimated to scale as

$$\begin{cases} V \propto V_1 \epsilon = \sqrt{3} c \lambda_z^{th} \epsilon & if \;\; \mathbf{Case(1)} : \frac{L_{ec}}{R_0} = constant \\ V \propto V_1 \epsilon = c\sqrt{\frac{8R_0}{L_{ec}}} \epsilon & if \;\; \mathbf{Case(2)} : \lambda_z = 1 \end{cases} \tag{41}$$

where the first case has been derived taking into account the definition of q in Equation (26), whilst the second arises from the dispersion relation in Equation (37). Therefore, we can introduce a slow temporal variable τ for the near-critical wave such that $\tau = \epsilon \frac{t}{\tau_c}$, where $\tau_c = \frac{l_c}{V_1}$ with l_c being the characteristic length of the problem, taken equal to R_0 in both the cases. Accordingly, the stream function can be rewritten as:

$$\phi\left(R, z, t\right) \rightarrow \phi\left(R, z, \epsilon \frac{t}{\tau_c}\right) \tag{42}$$

Assuming a series expansion in ϵ, the stream function can be expressed as:

$$\phi\left(R,z,\tau\right)=\phi_0\left(R,z\right)+\sum_{n=1}^{\infty}\epsilon^n\phi_n\left(R,z,\tau\right) \tag{43}$$

where the term ϕ_1 is written in analogy to the linear term in Equation (23), while the higher orders are built by resonating the lower orders as follows:

$$\begin{cases}\phi_1=Ru\left(\frac{R}{\sqrt{\lambda_z}}\right)A\left(\tau\right)e^{\mathbb{I}kz}+c.c.\\ \phi_2=R\left(G\left(\frac{R}{\sqrt{\lambda_z}}\right)\left|A\left(\tau\right)\right|^2+g\left(\frac{R}{\sqrt{\lambda_z}}\right)\mathbb{I}e^{2\mathbb{I}kz}A\left(\tau\right)^2\right)+c.c.\\ \phi_3=R\left(H\left(\frac{R}{\sqrt{\lambda_z}}\right)e^{\mathbb{I}kz}A\left(\tau\right)\left|A\left(\tau\right)\right|^2+h\left(\frac{R}{\sqrt{\lambda_z}}\right)e^{3\mathbb{I}kz}A\left(\tau\right)^3\right)+c.c.\end{cases} \tag{44}$$

In this multiple-scale approach, the temporal dependence is now absorbed by the complex variable $A\left(\tau\right)$ that describes the weakly non-linear amplitude of the perturbation just above the linear threshold, which will be fixed by the weakly non-linear effects.
The expression of all the scalar functions in Equation (44) will be derived solving the series expansion of the relative bulk and surface Euler-Lagrange equations. Since the beading instability occurs for $\bar{k}\to 0$, we will expand such equation up to the leading order in $\bar{k}$, i.e. the fifth for the Case (1) and the seventh for the Case (2). Accordingly, the hypothesis under this choice is to consider a cylinder of small aspect ratio, that means the length of the cylinder is much larger than its radius, $\bar{k}=2\pi R_0/L\ll 1$. In the following subsections, we will derive (i) the series expansions of bulk and surface Euler-Lagrange equations and (ii) their general solutions. For sake of simplicity, the coefficients in the expression of the functions u, G, g, H and h will be reported in the A. All the algebraic expressions presented in the following are derived using the software *Mathematica 9.0* (Wolfram Research, Champaign, Illinois).

4.1 Higher order solutions for the stream function in Case (1)

Let us first derive the the higher order solutions for the stream function in Equation (44) for the experimental situation described in Case (1).

4.1.1 Second order solution of the stream function

At the second order in ϵ, the bulk Euler-Lagrange equation in the term $|A|^2$ yields to

$$\mathcal{L}_0^2\left(G\right)=0 \tag{45}$$

where $\mathcal{L}_0=\frac{\partial^2}{\partial r^2}+\frac{1}{r}\frac{\partial}{\partial r}-\frac{1}{r^2}$ is the Laplacian operator in cylindrical coordinates, whose solution is:

$$G=C_4r^3+C_2r+\frac{C_1}{r}+C_3r\log r \tag{46}$$

Since the function G must be regular in $r=0$ and should satisfy the correspondent surface Euler-Lagrange equation, coefficients C_1, C_2, C_3 and C_4 must vanish so that there is no contribution at this order.
The second-order bulk Euler-Lagrange equation in the term $\mathbb{I}e^{2\mathbb{I}kz}A^2$ reads

$$\mathcal{L}_{1,2}\left[\mathcal{L}_{q,2}\left(g\right)\right]+\frac{k^5\sqrt{\lambda_z}\left(\lambda_z^3-1\right)^2\left(12\lambda_z^3+7\right)r}{2r_0^2}+O(k^5)=0 \tag{47}$$

The solution of this fourth order differential equation can be written as summation of a homogeneous solution, which is similar to the first order solution but with a wavelength doubling, and the particular solution. Imposing regularity in $r = 0$, the solution reads:

$$g = \alpha_2 \frac{I_1\left(2kr\lambda_z^{3/2}\right)}{I_1\left(2kr_0\lambda_z^{3/2}\right)} + \beta_2 \frac{I_1(2kr)}{I_1(2kr_0)} - \frac{k\left(-12\lambda_z^9 + 17\lambda_z^6 + 2\lambda_z^3 - 7\right) r}{32\lambda_z^{5/2} r_0^2} \tag{48}$$

where α_2 and β_2 are two constants to be determined from the following two surface conditions given by

$$\begin{cases} \gamma\lambda_z \left(128k^2\lambda_z^{5/2} r_0^3(\alpha_2+\beta_2) - 32\lambda_z^{5/2} r_0(\alpha_2+\beta_2) \right. \\ +14k^3\left(\lambda_z^3-1\right)^2\left(3\lambda_z^3+2\right) r_0^2 - k\left(\lambda_z^3-1\right)^2\left(6\lambda_z^3+7\right)\Big) \\ +2\mu r_0 \left(16k^2\lambda_z^{5/2} r_0^3\left(\lambda_z^3(2\alpha_2+\beta_2)+\beta_2\right) + 32\lambda_z^{5/2} r_0\left(\alpha_2+\beta_2\lambda_z^3\right)\right. \\ \left. +k^3\left(\lambda_z^3-1\right)^2\left(3\lambda_z^3+5\right)\lambda_z^3 r_0^2 + k\left(\lambda_z^3-1\right)^2\left(15\lambda_z^3+7\right)\right) = 0 \\ \\ \alpha_2\left(\lambda_z^3+1\right) + 2\beta_2 + \frac{k\left(\lambda_z^3-1\right)^2\left(\lambda_z^3\left(16-k^2r_0^2\right)+7\right)}{\lambda_z^{5/2} r_0} = 0 \end{cases} \tag{49}$$

The third order solution for the stream function will be derived in the next paragraph.

4.1.2 Third order solution of the stream function

At the third order in ϵ, the bulk Euler-Lagrange equation in the term $e^{\mathbb{I}kz} A\left|A\right|^2$ is given by:

$$\mathcal{L}_{1,1}\left[\mathcal{L}_{q,1}\left(H\right)\right] = 0 \tag{50}$$

This equation admits the same solution proposed for Equation (24); than, it can be written as

$$H = \alpha_{31} \frac{I_1\left(kr\lambda_z^{3/2}\right)}{I_1\left(kr_0\lambda_z^{3/2}\right)} + \beta_{31} \frac{I_1\left(kr\right)}{I_1\left(kr_0\right)} \tag{51}$$

The two boundary conditions to determine the coefficients α_{31} and β_{31} are

$$\begin{cases} \gamma^2\lambda_z^2\left(8r_0^2(\alpha_{31}+\beta_{31}) - k^2\left(8r_0^4(\alpha_{31}+\beta_{31}) + 3\lambda_z^{10} - 9\lambda_z^7 + 9\lambda_z^4 - 3\lambda_z\right)\right) \\ +\gamma\lambda_z\mu r_0\left(k^2\left(2\lambda_z^3 r_0^4(6\alpha_{31}+7\beta_{31}) + 2r_0^4(16\alpha_{31}+15\beta_{31})\right.\right. \\ \left. +27\lambda_z^{13} - 57\lambda_z^{10} + 9\lambda_z^7 + 45\lambda_z^4 - 24\lambda_z\right) \\ \left. -16r_0^2\left(\alpha_{31}\left(\lambda_z^3+3\right) + 2\beta_{31}\left(\lambda_z^3+1\right)\right)\right) \\ +4\mu^2 r_0^2\left(k^2\left(\lambda_z^6 r_0^4(2\alpha_{31}+\beta_{31}) + \lambda_z^3 r_0^4(4\alpha_{31}+3\beta_{31})\right.\right. \\ \left. +2\beta_{31}r_0^4 - 6\lambda_z^{16} - 24\lambda_z^{13} + 108\lambda_z^{10} - 120\lambda_z^7 + 42\lambda_z^4\right) \\ \left. +8\left(\lambda_z^3+2\right) r_0^2\left(\alpha_{31}+\beta_{31}\lambda_z^3\right)\right) = 0 \\ \\ \gamma\lambda_z\left(3k^2\lambda_z\left(\lambda_z^3-1\right)^3 - 8r_0^2\left(\alpha_{31}\lambda_z^3+\alpha_{31}+2\beta_{31}\right)\right) \\ +4\mu r_0\left(4\left(\lambda_z^3+2\right) r_0^2\left(\alpha_{31}\lambda_z^3+\alpha_{31}+2\beta_{31}\right) - 3k^2\lambda_z^4\left(\lambda_z^3-1\right)^3\right) = 0 \end{cases} \tag{52}$$

The third-order bulk Euler-Lagrange equation in the term $e^{3\mathbb{I}kz}A^3$ reads:

$$\mathcal{L}_{1,3}\left[\mathcal{L}_{q,3}\left(h\right)\right]=0 \tag{53}$$

whose solution is:

$$h=\alpha_3\frac{I_1\left(3kr\lambda_z^{3/2}\right)}{I_1\left(3kr_0\lambda_z^{3/2}\right)}+\beta_3\frac{I_1\left(3kr\right)}{I_1\left(3kr_0\right)} \tag{54}$$

where the regularity of the function in $r=0$ is already considered by dropping off the dependence on the Bessel function of second kind K_1. Finally, the two surface conditions impose

$$\begin{cases}
2\gamma^2\lambda_z^2\left(k^2\left(108r_0^4(\alpha_3+\beta_3)+\lambda_z^{10}-3\lambda_z^7+3\lambda_z^4-\lambda_z\right)-12r_0^2(\alpha_3+\beta_3)\right)\\
+\gamma\lambda_z\mu r_0\left(48r_0^2\left(\alpha_3\left(\lambda_z^3+3\right)+2\beta_3\left(\lambda_z^3+1\right)\right)\right.\\
\left.-k^2\left(54\lambda_z^3r_0^4(6\alpha_3+7\beta_3)+54r_0^4(16\alpha_3+15\beta_3)+15\lambda_z^{13}-49\lambda_z^{10}+57\lambda_z^7-27\lambda_z^4+4\lambda_z\right)\right)\\
-4\mu^2r_0^2\left(k^2\left(27\lambda_z^6r_0^4(2\alpha_3+\beta_3)+27\lambda_z^3r_0^4(4\alpha_3+3\beta_3)\right.\right.\\
\left.\left.+54\beta_3r_0^4-10\lambda_z^{16}+40\lambda_z^{13}-60\lambda_z^{10}+40\lambda_z^7-10\lambda_z^4\right)\right.\\
\left.+24\left(\lambda_z^3+2\right)r_0^2\left(\alpha_3+\beta_3\lambda_z^3\right)\right)=0\\
\\
4\mu r_0\left(4\left(\lambda_z^3+2\right)r_0^2\left(\alpha_3\lambda_z^3+\alpha_3+2\beta_3\right)+k^2\left(\lambda_z^3-1\right)^3\lambda_z^4\right)\\
-\gamma\lambda_z\left(8r_0^2\left(\alpha_3\lambda_z^3+\alpha_3+2\beta_3\right)+k^2\lambda_z\left(\lambda_z^3-1\right)^3\right)=0
\end{cases} \tag{55}$$

which allow to determine the two coefficients α_3 and β_3.

4.2 Higher order solutions for the stream function in Case (2)

In the following, we will derive the higher order solutions for the stream function in Equation (44) for the experimental situation described in Case (2).

4.2.1 Second order solution of the stream function

At the second order in ϵ, the boundary value problem in the term $|A|^2$ is the same as for Case (1), so it is found that $G=0$.
The second-order bulk Euler-Lagrange equation in the term $\mathbb{I}e^{2\mathbb{I}kz}A^2$ reads:

$$\mathcal{L}_{1,2}^2\left(g\right)-19k^7r+O(k^7)=0 \tag{56}$$

Again, the solution of this fourth order differential equation is given by the sum of the homogeneous and the particular solutions, being:

$$g=\alpha I_1\left(2kr\right)+\beta\left[K_1\left(2kr\right)\int_0^r rI_1^2\left(2kr\right)dr-I_1\left(2kr\right)\int_0^r rI_1\left(2kr\right)K_1\left(2kr\right)dr\right]+\frac{19}{32}k^3r \tag{57}$$

The constants α_2 and β_2 can be determines from the two following boundary conditions:

$$\begin{cases} 48\alpha_2 k^3 \left(\gamma \left(23k^4 r_0^4 + 42k^2 r_0^2 - 12\right) + 2\mu r_0 \left(5k^4 r_0^4 + 18k^2 r_0^2 + 12\right)\right) \\ -3\gamma \left(k^7 r_0^2 \left(31\beta_2 r_0^4 - 411\right) + k^5 \left(88\beta_2 r_0^4 + 78\right) - 24\beta_2 k^3 r_0^2\right) \\ +2k\mu r_0 \left(36k^4 \left(6k^2 r_0^2 + 11\right) - \beta_2 \left(17k^6 r_0^6 + 84k^4 r_0^4 + 72k^2 r_0^2 - 144\right)\right) = 0 \\ \\ -\frac{1}{144} k^7 \mu r_0^3 \left(-96\alpha_2 r_0^2 + 7\beta_2 r_0^4 + 36\right) - \frac{1}{24} k^5 \mu r_0 \left(-96\alpha_2 r_0^2 + 10\beta_2 r_0^4 - 69\right) \\ +k^3 \left(8\alpha_2 \mu r_0 - \frac{3}{2}\beta_2 \mu r_0^3\right) - \beta_2 k \mu r_0 = 0 \end{cases} \tag{58}$$

The third order solution for the stream function will be derived in the next paragraph.

4.2.2 Third order solution of the stream function

At the third order in ϵ, the bulk Euler-Lagrange equation in the term $e^{\mathbb{I}kz} A |A|^2$ rewrites:

$$\mathcal{L}^2_{1,1}(H) = 0 \tag{59}$$

whose solution, after imposing the regularity in $r = 0$, is given by:

$$H = \alpha_{31} I_1(kr) + \beta_{31} \left[K_1(kr) \int_0^r r I_1^2(kr)\, dr - I_1(kr) \int_0^r r I_1(kr) K_1(kr)\, dr \right] = 0 \tag{60}$$

The boundary conditions from the surface Euler-Lagrange equations read:

$$\begin{cases} -48\alpha_{31} k^2 \left(\gamma^2 \left(23k^4 r_0^4 + 168k^2 r_0^2 - 192\right) - 32\gamma\mu r_0 \left(4k^4 r_0^4 + 27k^2 r_0^2 - 48\right) - 12\mu^2 r_0^2 \left(5k^4 r_0^4 + 72k^2 r_0^2 + 192\right)\right) \\ +3\gamma^2 \left(k^6 \left(31\beta_{31} r_0^6 + 2304\right) + 352\beta_{31} k^4 r_0^4 - 384\beta_{31} k^2 r_0^2\right) \\ -4\gamma\mu r_0 \left(\beta_{31} \left(131k^6 r_0^6 + 1416k^4 r_0^4 - 2304k^2 r_0^2 + 4608\right) + 29376k^6\right) \\ -12\mu^2 r_0^2 \left(\beta_{31} \left(17k^6 r_0^6 + 336k^4 r_0^4 + 1152k^2 r_0^2 - 9216\right) - 36864k^6\right) = 0 \\ \\ 96k^2 \left(\alpha_{31} \left(k^4 r_0^4 + 24k^2 r_0^2 + 192\right)(\gamma - 6\mu r_0) + 72k^4 (\gamma - 4\mu r_0)\right) \\ -\beta_{31} \left(7k^6 r_0^6 + 240k^4 r_0^4 + 3456k^2 r_0^2 + 9216\right)(\gamma - 6\mu r_0) = 0 \end{cases} \tag{61}$$

which allow to determine the coefficients α_{31} and β_{31}.
The third-order bulk Euler-Lagrange equation in the term $e^{3\mathbb{I}kz} A^3$ reads:

$$\mathcal{L}^2_{1,3}(g) = 0 \tag{62}$$

whose regular solution is:

$$h = \alpha_3 I_1(3kr) + \beta_3 \left[K_1(3kr) \int_0^r r I_1^2(3kr)\, dr - I_1(3kr) \int_0^r r I_1(3kr) K_1(3kr)\, dr \right] \tag{63}$$

The corresponding surface conditions are given by:

$$\begin{cases} 144\alpha_3 k^2\left(\gamma^2\left(621k^4r_0^4+504k^2r_0^2-64\right)-32\gamma\mu r_0\left(108k^4r_0^4+81k^2r_0^2-16\right)\right. \\ \left.-12\mu^2r_0^2\left(135k^4r_0^4+216k^2r_0^2+64\right)\right) \\ +\gamma^2\left(-\left(k^6\left(7533\beta_3r_0^6+512\right)+9504\beta_3k^4r_0^4-1152\beta_3k^2r_0^2\right)\right) \\ +4\gamma\mu r_0\left(\beta_3\left(10611k^6r_0^6+12744k^4r_0^4-2304k^2r_0^2+512\right)+704k^6\right) \\ +12\beta_3\mu^2r_0^2\left(1377k^6r_0^6+3024k^4r_0^4+1152k^2r_0^2-1024\right)=0 \\ \\ -7776\alpha_3\gamma k^6r_0^4-20736\alpha_3\gamma k^4r_0^2-18432\alpha_3\gamma k^2+46656\alpha_3k^6\mu r_0^5 \\ +124416\alpha_3k^4\mu r_0^3+110592\alpha_3k^2\mu r_0+567\beta_3\gamma k^6r_0^6+2160\beta_3\gamma k^4r_0^4 \\ +3456\beta_3\gamma k^2r_0^2-1296\beta_3k^4r_0^4\left(21k^2r_0^2+8\right)\log(r_0)(\gamma-6\mu r_0) \\ +648\beta_3k^4r_0^4\left(21k^2r_0^2+8\right)\log\left(r_0^2\right)(\gamma-6\mu r_0)+1024\beta_3\gamma-3402\beta_3k^6\mu r_0^7 \\ -12960\beta_3k^4\mu r_0^5-20736\beta_3k^2\mu r_0^3-6144\beta_3\mu r_0+768\gamma k^6-3072k^6\mu r_0=0 \end{cases} \tag{64}$$

which allow determining the coefficients α_3 and β_3.

5 Derivation of the Ginzburg-Landau equations

The weakly non-linear analysis aims at deriving the evolution equations for the amplitude of the near-critical waves, also known as *Ginzburg-Landau* equations. The classical method would consist in calculating the higher order solutions of the stream function until a solvability condition on the amplitude $A(\tau)$ must be imposed in order to avoid the presence of secular terms. Since this would require lengthy calculation, an alternative approach based on energetic consideration will be used in the following. In fact, since we deal with a conservative system, the Lagrangian functional $\mathcal{L}$ is invariant with respect to time, thus the Noether's theorem states that the total energy of the system is a conserved quantity [32]. Therefore, the time derivative of the total mechanical energy E must vanish, so that:

$$\frac{dE}{dt}=0\rightarrow\frac{\partial}{\partial\tau}\left(\int_{\bar{\Omega}}\left(K+\Psi_e\right)d\bar{\Omega}+\int_{\bar{\Gamma}}\left(\Psi_s\right)d\bar{\Gamma}\right)=0 \tag{65}$$

which allows deriving the Ginzburg-Landau equations for the amplitudes of the near-critical waves. Indeed, let us consider a series expansion of E in ϵ up to the fourth order as

$$E\left(u,g,H\right)=E_0\left(u\right)+\sum_{n=1}^{4}\epsilon^nE_n\left(u,g,H\right) \tag{66}$$

where E_n are the coefficients of the energy series expansion, which depend on the scalar function u, g and H calculated in the previous Sections. In particular it is found that:

- the term E_0 is a constant, representing the energy of the basic homogeneous solution:

$$E_0=\frac{\pi\mu R_0^2}{k\left(\lambda_z^{th}\right)^2}\left(1-\frac{3\lambda_z^{th}}{2}+\frac{\left(\lambda_z^{th}\right)^3}{2}\right)+\frac{2\pi\gamma R_0}{k\lambda_z^{th}} \tag{67}$$

- the terms E_1 and E_3 vanish because of the periodicity;
- the term E_2 is null because it reduces to the incremental power of the first-order solution [16];
- the term E_4 reads:

$$E_4 = \kappa \left| \frac{dA(\tau)}{d\tau} \right|^2 + \nu |A(\tau)|^2 - \frac{\psi}{2} |A(\tau)|^4 \tag{68}$$

Taking the time derivative of total energy E the Ginzburg-Landau equations for the amplitude evolution of the near-critical modes become [22]:

$$\kappa \frac{d^2 A(\tau)}{d\tau^2} + \nu A(\tau) - \psi |A(\tau)|^2 A(\tau) = 0 \tag{69}$$

where $\kappa = \int_0^{R_0} \gamma_v dR$, $\psi = -\left(\int_0^{R_0} \alpha_v dR + \alpha_s \right)$, $\nu = \int_0^{R_0} \beta_v dR + \beta_s$ and the complex conjugate equation also exists. The expression of the coefficients γ_v, α_v, β_v, α_s, β_s in Equation (68) are reported in B. The static solution A^{st} of Equation (69) is:

$$A^{st} = \sqrt{\frac{\nu}{\psi}} \tag{70}$$

Accordingly, if $\frac{\nu}{\psi} > 0$ then the static solution is stable, and the pitchfork bifurcation is supercritical, meaning that the beading amplitude grows continuously as the square root of the distance from the threshold value of the order parameter. Conversely, if $\frac{\nu}{\psi} < 0$ the static solution is unstable and the pitchfork bifurcation is subcritical. Thus, we expect that the beading amplitude might have a discontinuity after the marginal stability threshold, which is controlled by non-linear effects of higher orders.
Table 1 collects the numerical results for the coefficients in Equation (69) for several choices of the geometrical and material parameters for the Case (1) and Case (2), also indicating the nature of bifurcation.

Case (1): varying λ_z; fixed $\frac{L_{ec}}{R_0}$

$\left(\frac{L_{ec}}{R_0}\right)$	$\frac{L_0}{R_0}$	$\bar{k}$	λ_z^{th}	A^{st}
	628	0.01	1.0372	$1.762\mathbb{I}$ (sub)
5.9	62.8	0.1	1.0619	$1.142\mathbb{I}$ (sub)
	31.4	0.2	1.1675	0.151 (super)

Case (2): varying $\frac{L_{ec}}{R_0}$; fixed $\lambda_z = 1$

λ_z	$\frac{L_0}{R_0}$	$\bar{k}$	$\left(\frac{L_{ec}}{R_0}\right)^{th}$	A^{st}
	6283.19	0.001	6.00001	$0.139\mathbb{I}$ (sub)
1	628.32	0.01	6.0001	0.461 (super)
	125.67	0.05	6.0151	5.696 (super)

Table 1: Numerical values for the static solution A^{st} for Case (1) and Case (2) calculated from the weakly non-linear analysis for selected values of $\bar{k}$ and, hence, of L_0/R_0. The corresponding type of bifurcation is indicated in brackets (sub= subcritical, super=supercritical). We set $\frac{L_{ec}}{R_0} = 5.9$ for the Case (1), and $\lambda_z = 1$ for the Case (2).

6 Numerical simulations of the post-buckling behaviour

In the theoretical part of this work we performed both a linear and a weakly non-linear stability analysis for the beading of an axially stretched elastic soft cylinder, having a surface tension such that its elastocapillary length is comparable to its radius. In this Section, we propose a numerical investigation having a two-fold purpose: first, validating the analytical results; second, performing numerical simulations to investigate the fully non-linear beading morphology far beyond the linear stability threshold.

6.1 Description of the numerical model

The numerical model is implemented by using the open source tool for solving partial differential equations *FEniCS* [31]. We modelled a two-dimensional axisymmetric cylinder of initial length L_0 and radius R_0. Periodic boundary conditions for the radial displacement are imposed on the extremities of the geometry. A non-linear elastic neo-Hookean material having a given surface tension is taken into account, using the potential energies in Equation (3). Since the theoretical analysis predicted that the critical wave is stationary, i.e. $V = 0$, a quasi-static simulation has been performed. In order to exactly enforce the incompressibility constraint, a mixed formulation with triangular Taylor-Hood elements (maximum of 4000 elements) has been implemented: the displacements in the two orthogonal directions are approximated by continuous piecewise quadratic functions whereas the pressure by continuous piecewise linear function. The solution has been found through an incremental iterative Newton-Raphson method and, in each iteration, the calculation are conducted by using the linear algebra back-end PETSc (Portable, Extensible Toolkit for Scientific Computation) and the linear system is solved through a LU (Lower-Upper) decomposition.

Figure 2 depicts an example of the implemented geometry and the mesh used for the simulations: although the model is axisymmetric, a three-dimensional rendering is also presented for sake of clarity.

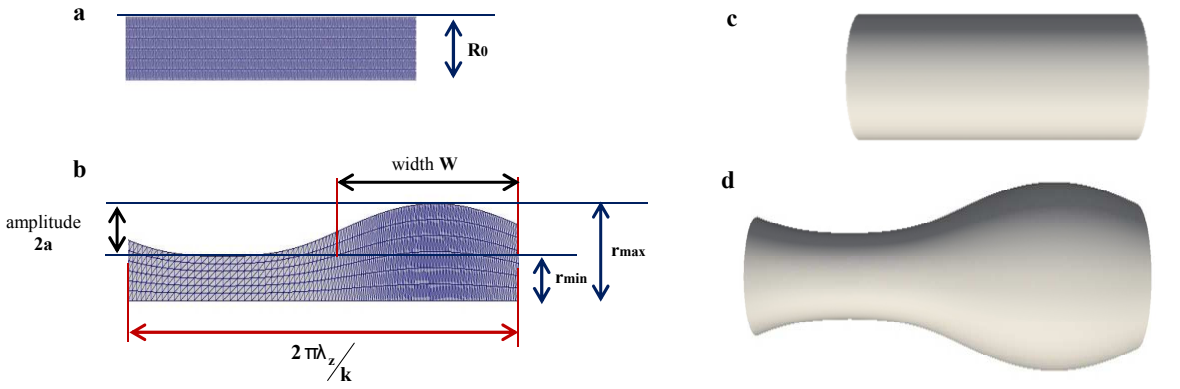

Figure 2: Example of geometry and mesh of the numerical model. (a) Undeformed 2D mesh; (b) deformed 2D mesh; (c) 3D rendering of undeformed sample; (d) 3D rendering of the deformed sample. In (b) the beading amplitude $a = \frac{r_{max}-r_{min}}{2}$ and bead width w, computed as the length of the portion of the cylinder whose radius r is such that $r > \frac{r_{max}+r_{min}}{2}$, are shown. We also define the normalized width as $\bar{w} = \frac{w}{\lambda_z(2\pi/k)}$.

According to the choice of the control parameters for the two cases under investigation, the simulations have been performed by increasing the stretch λ_z (Case (1)) and by decreasing the shear modulus μ (Case (2)).

6.2 Validation of the theoretical predictions

The validation of the theoretical results is performed comparing the prediction and the numerical outputs on two quantities: (i) the linear threshold computed for the selected conditions presented in Tables 2 and 3 of the Appendix B for both cases (1) and (2); (ii) the weakly non-linear predictions for the wave amplitude computed for selected supercritical conditions in the Case (2).

6.2.1 Comparison between the theoretical and the numerical linear stability thresholds

Let us first validate our finite element code by comparing the numerical results with the predictions of the linear stability analysis. For this purpose, we introduce a sinusoidal imperfection in the mesh of the undeformed cylinder having the first unstable wavenumber predicted by our theoretical results and an amplitude of $1/100$ of the initial radius R_0.
The comparison of the linear stability threshold is performed by calculating the ratio between the total energy E_{num} in the simulated cylinder with respect to the homogeneous basic solution E_0. As depicted in Figure 3, the simulations, that are performed for selected conditions presented in Tables 2 and 3, predict very well the theoretical linear stability thresholds against λ_z and $\frac{L_{ec}}{R_0}$. The numerical thresholds are calculated as the values of the control parameters at which the ratio $(E_{num} - E_0)/E_0 = 10^{-5}$.

6.2.2 Comparison between the theoretical and the numerical results for the weakly non-linear beading amplitude

Let us now compare the theoretical predictions of the weakly non-linear stability analysis with the results of the numerical simulations. In particular, we compare the amplitude of the beaded cylinders arising from the static solution of the Ginzburg-Landau equation in (70) with the resulting morphology in simulations. As depicted in Figure 2, the weakly non-linear amplitude a of the supercritical beading theoretically scales beyond the linear stability thresholds as:

$$a \sim 2ku|_{R=R_0} A^{st} \epsilon \tag{71}$$

where Equation (13) has been used.
It is found that the amplitude of the perturbation computed through the numerical model (dotted lines) fits very well with the theoretical predictions (dashed lines) in the weakly non-linear regime, as shown in Figure 4. Four different choices of $\bar{k}$ have been considered for the Case (2) corresponding to supercritical bifurcations.

6.3 Fully non-linear beading and phase diagrams

Once that the numerical code has been validated with the theoretical predictions of the linear and the weakly non-linear stability analysis, we use it to evaluate the fully non-linear beading of the soft cylinder. In Figure 5(a), we first compare the amplitude of the beading computed

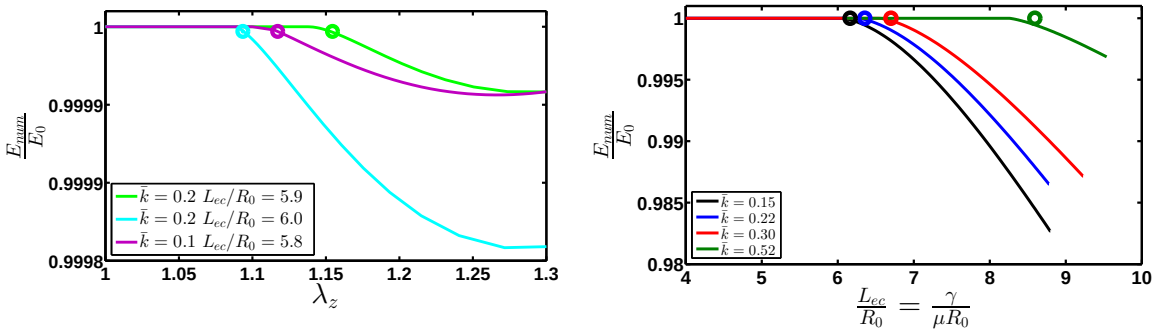

(a) (b)

Figure 3: (a) Normalized energy plots in function of the control parameter λ_z for three selected choices of $\bar{k}$ and $\frac{L_{ec}}{R_0}$ collected in Table 2. (b) Normalized energy plots in function of the elastocapillary ratio $\frac{L_{ec}}{R_0}$ for four selected choices of $\bar{k}$ collected in Table 3. Circles indicate the theoretical predictions. In the two cases, theoretical and simulated linear stability thresholds are reported below. (a) $\lambda^{th}_{z,theo} = 1.168$ - $\lambda^{th}_{z,sim} = 1.154$ (light green line); $\lambda^{th}_{z,theo} = 1.097$ - $\lambda^{th}_{z,sim} = 1.093$ (cyan line); $\lambda^{th}_{z,theo} = 1.118$ - $\lambda^{th}_{z,sim} = 1.117$ (magenta line). (b) $\left(\frac{L_{ec}}{R_0}\right)^{th}_{theo} = 6.16$ - $\left(\frac{L_{ec}}{R_0}\right)^{th}_{sim} = 6.04$ (black line); $\left(\frac{L_{ec}}{R_0}\right)^{th}_{theo} = 6.36$ - $\left(\frac{L_{ec}}{R_0}\right)^{th}_{sim} = 6.24$ (blue line); $\left(\frac{L_{ec}}{R_0}\right)^{th}_{theo} = 6.69$ - $\left(\frac{L_{ec}}{R_0}\right)^{th}_{sim} = 6.49$ (red line); $\left(\frac{L_{ec}}{R_0}\right)^{th}_{theo} = 8.64$ - $\left(\frac{L_{ec}}{R_0}\right)^{th}_{sim} = 8.22$ (dark green line).

through the fully non-linear simulation with the experimental results presented in Mora et al. [35], that are of the type investigated into Case (2). The critical wavenumbers of the beading are $\bar{k} = 0.15$ and $\bar{k} = 0.22$, corresponding to $n_f = 2$ and $n_f = 3$, respectively, for the experimental geometry of a gel fibre with $L_0 = 20mm$ and $R_0 = 0.24mm$. In both cases the bifurcation is found to be supercritical, i.e. characterized by a continuous increase of the beading amplitude beyond the linear stability threshold.
In Figure 5(b) we show the evolution of the beading amplitude for a condition taken from Case (2), when the fibre is subjected to a cyclical change of the order parameter μ. Shortly beyond the first supercritical bifurcation at around $\mu = 18.5Pa$ ($\bar{k} = 0.52$ in Table 3), we find a second subcritical bifurcation at around $\mu = 18.4Pa$ characterized by both a sudden jump and an hysteresis of the beading amplitude.

Finally, in Figure 6 we provide a quantitative measure of the beading amplitude a and the normalized width $\bar{w}$ for both the cases. In particular, Figure 6(a) show that, for Case (1), the amplitude first grows as the square root of the distance from the stretch thresholds, then saturates at a constant value, until the beading is completely recovered by further increasing the finite axial stretch. In Figure 6(b), we report the same geometrical results for the Case (2) in function of the ratio between the elastocapillary length and the cylinder radius. Beyond the linear stability threshold ($L_{ec} = 6.14R_0$ in the presented condition), the amplitude grows continuously while the morphology evolves towards a bead-on-a-string structure. The numerical simulations permit to extract a qualitative representation of the deformed morphologies, as presented under the corresponding plots.

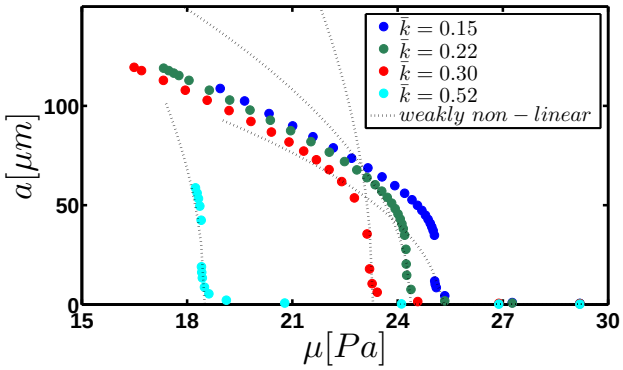

Figure 4: Amplitude evolution of the perturbation for four different $\bar{k}$ investigated in the Case (2). Dashed lines indicate the theoretical predictions in the nearby of the linear thresholds, given by Equation (71). The comparison between numerical and theoretical results is performed in the range $\left[0.98\mu_{sim}^{th} - \mu_{sim}^{th}\right]$: $SSE = 2.48 \cdot 10^{-5}$ (blue dots); $SSE = 1.57 \cdot 10^{-4}$ (green dots); $SSE = 1.25 \cdot 10^{-3}$ (red dots); $SSE = 3.67 \cdot 10^{-3}$ (cyan dots)

7 Imperfection sensitivity analysis

The linear and the weakly non-linear analysis for the Case (1) have shown that: (i) in the limit $\bar{k} \to 0$, the linear thresholds in terms of the axial stretch are very close each others for different wavenumbers, with critical value being $\bar{k} = 2\pi R_0/L_0$; (ii) in such cases, the bifurcation is found to be subcritical. It is well known in stability problems of elastic structures that subcritical bifurcations are very sensitive to surface imperfections [8, 10] implying that the evolution of the imperfect system might differs significantly from the perfect case. In order to quantify this effect on the beading onset and evolution, we perform in this Section an imperfection sensitivity analysis on the stretched cylinder.
Let us consider an initial imperfection in the soft cylinder such that the radial coordinate R is given by

$$R \in \left[0, R_0 + \xi^2 \frac{2\pi}{k_{imp}} \left(e^{\mathbb{I} k_{imp} z} + e^{-\mathbb{I} k_{imp} z}\right)\right] \tag{72}$$

where k_{imp} represents the wavenumber of the initial surface imperfection and $\xi \ll 1$ a small parameter fixing its initial amplitude. In order to investigate the interaction between the imperfection mode and all the possible near-critical modes at the linear order, we can rewrite the stream function $\phi(R, z, \tau)$ in form of Fourier summation as

$$\phi(z, R, \tau) = \phi_0 + \xi \psi_1(z, R, \tau) \tag{73}$$

with

$$\psi_1(z, R, t) = \sum_{n \neq 0} A_n(\tau)\, R U_n e^{I k_{imp} n z} \tag{74}$$

where n is an integer number representative of the generic wavenumber such that $k^* = |n k_{imp}|$, $A_n(\tau)$ is the amplitude of the $n-th$ mode, so that A_{-n} is the complex conjugate of A_n, and U_n the linear solution u found in Section 3.1 for the corresponding wavenumber k^*. As done for the previous weakly non-linear analysis in the perfect system, the evolution equations can

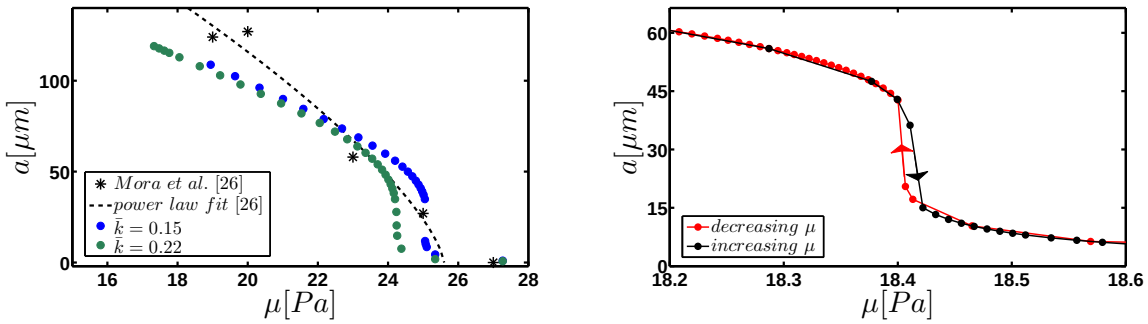

(a) (b)

Figure 5: (a) Comparison between the experimental data presented in Mora et al. [35] and the results of our numerical simulations. The star markers indicate the experimental values, whereas the results of two corresponding simulations are reported as green and blues dotted lines. The dashed line indicates the power law fit proposed in Mora et al. [35], i.e. $a = 34.1\,(25.6-\mu)^{0.71}$ (b) Beading amplitude for a decreasing value of shear modulus μ (red line) and for its subsequent increasing (black line): the supercritical bifurcation predicted by the weakly non-linear analysis (at $\mu = 18.5Pa$) is followed by a secondary subcritical bifurcation (at about $\mu = 18.4Pa$) with a sudden jump and an hysteresis of a.

be found by imposing the conservation of the total energy. Accordingly, the total mechanical energy E for such an imperfect system rewrites:

$$\begin{aligned} E &= \int_0^{\frac{2\pi}{k_{imp}}} \int_0^{R_0+\xi^2\zeta(z)} (K+W)\,\Phi_{,Rz}\,dRdz + \int_0^{\frac{2\pi}{k_{imp}}} E_{sup}|_{R=R_0+\xi^2\zeta(z)} \\ &\approx \int_0^{\frac{2\pi}{k_{imp}}} \int_0^{R_0} (K+W)\,\Phi_{,Rz}\,dRdz + \int_0^{\frac{2\pi}{k_{imp}}} \xi^2\zeta(z)\,|(K+W)\,\Phi_{,Rz}|_{R=R_0} + \int_0^{\frac{2\pi}{k_{imp}}} E_{sup}|_{R=R_0+\xi^2\zeta(z)} \end{aligned} \tag{75}$$

where $\zeta(z) = \frac{2\pi}{k_{imp}}\left(e^{\mathbb{I}k_{imp}z} + e^{\mathbb{I}k_{imp}z}\right)$. Let us consider the following scaling where α_{imp} of the order $O(1)$ indicates the increment of stretch:

$$\lambda_z = \lambda_{z0}\,(1-\xi\alpha_{imp})\,; \quad \tau = \sqrt{\xi\alpha_{imp}}\,\frac{t}{\tau_c} \tag{76}$$

and the slow time-scale τ has been derived using the same procedure shown in Equation (41). The series development up to the third order in ξ of the total mechanical energy E is derived

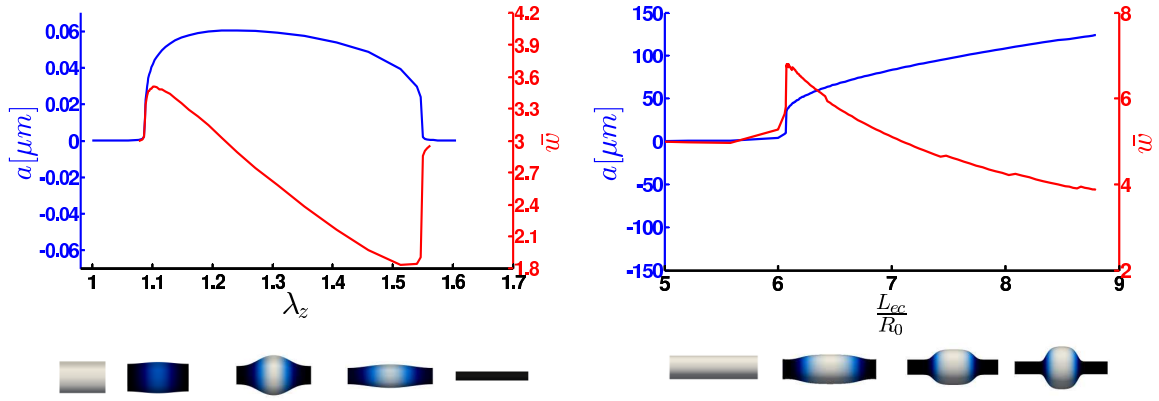

(a) (b)

Figure 6: (a) Amplitude (red line) and normalized width $\bar{w}$ (blue line) over the applied stretch in the Case (1), with $\frac{L_{cc}}{R_0} = 5.9$, $\bar{k} = 0.2$, $R_0 = 0.24\mu m$, $\mu = 20Pa$. (b) Amplitude (red line) and normalized width $\bar{w}$ (blue line) over the elastocapillary ratio in the Case (2), with $\bar{k} = 0.15$ and $R_0 = 0.2mm$.

as:

$$E = E_{b0} + E_{s0} + \xi\left(E_{b1} + E_{s1}\right) + \xi^2\left(E_{b2} + E_{s2}\right)$$
$$+ \xi^3\left[\sum_{n\neq 0}\left(\left(\nu_{n,b} + \nu_{n,s}\right)\left|\frac{\partial A_n(\tau)}{\partial \tau}\right|^2 + \left(\beta_{n,b} + \beta_{n,s}\right)\left|A_n(\tau)\right|^2\right.\right.$$
$$\left.\left. + \sum_{m\neq 0, m\neq n}\left(Q(m,n) + Q_s(m,n)\right)A_m(\tau)A_{n-m}(\tau)A_{-n}(\tau)\right) + B + \left(\omega_{1,b} + \omega_{1,s}\right)\left(A_1(\tau) - A_{-1}(\tau)\right)\right] \tag{77}$$

where the expressions of all the coefficients are presented in the C, and the subscripts b and s represent the contribution of the bulk and the surface terms, respectively. Imposing the conservation of the total mechanical energy, the following condition arises:

$$\frac{dE}{d\tau} = \sum_p\left[\frac{\partial E}{\partial A_p'}A_p''(\tau) + \frac{\partial E}{\partial A_p}A_p'(\tau)\right] = 0 \tag{78}$$

which results in an infinite number of Ginzburg-Landau equations for the near-critical modes, being:

$$2\nu_{p,b}A_p''(\tau) + 2\left(\beta_{p,b} + \beta_{p,s}\right)A_p(\tau) + \left(\omega_{1,b} + \omega_{1,s}\right)\left(\delta_{1,p} - \delta_{-1,p}\right)$$
$$+ \sum_{n\neq 0, n\neq p}\left[K(p,n)A_n(\tau)A_{p-n}(\tau)\right] = 0 \tag{79}$$

where $K(p,n) = Q(-n,-p) + Q(p,n) + Q(-n,p-n)$ and the orthogonality property of the integrals has been used.

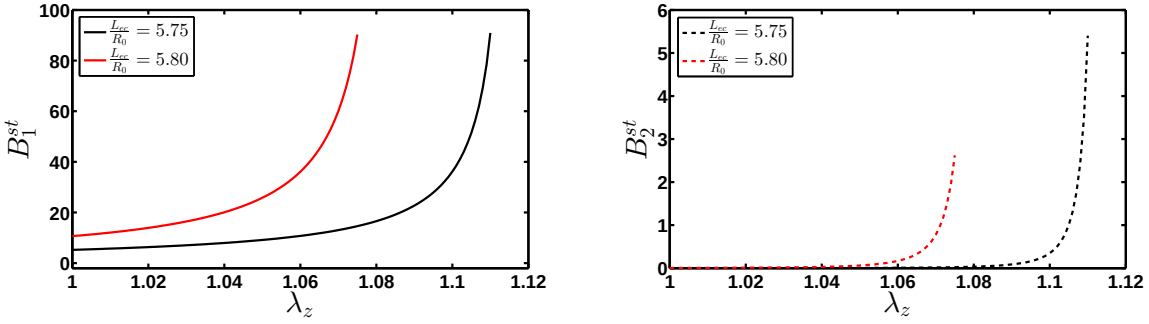

(a) (b)

Figure 7: Plot of the static amplitudes (a) B_1^{st} and (b) B_2^{st} over the applied stretch λ_z for $\frac{L_{ec}}{R_0}$ equal to 5.8 and 5.75. In both the cases, the cylinders have radius $R_0 = 0.2\mu m$ and a shear modulus $\mu = 20Pa$; the initial imperfection is set to $\xi = 0.0003$ with normalized wavenumber $k_{imp} = 0.01$.

This system of amplitude equations admits a solution in the form $A_p = \mathbb{I}B_p$, with B_p real and $B_{-p} = -B_p$, such that:

$$2\mathbb{I}\nu_{p,b}B_p''(\tau) + 2\mathbb{I}(\beta_{p,b} + \beta_{p,s})B_p(\tau) + (\omega_{1,b} + \omega_{1,s})(\delta_{1,p} - \delta_{-1,p}) - \sum_{n\neq 0, n\neq p}[K(p,n)B_n(\tau)B_{p-n}(\tau)] = 0 \tag{80}$$

In order to find the static solutions B^{st} for the amplitude modes, we must solve:

$$2\mathbb{I}(\beta_{p,b} + \beta_{p,s})B_p^{st} + (\omega_{1,b} + \omega_{1,s})(\delta_{1,p} - \delta_{-1,p}) - \sum_{n\neq 0, n\neq p}\left[K(p,n)B_n^{st}B_{p-n}^{st}\right] = 0 \tag{81}$$

As a first analysis, let us compute the two-mode approximation of the static solution, i.e. determining B_p^{st} for $p = 1, 2$ assuming that $B_p^{st} = 0$ if $p > 2$. Setting $p = 2$ in Equation (81),

$$B_2^{st} = \frac{K(2,1)}{2\mathbb{I}(\beta_{2,b} + \beta_{2,s})}\left(B_1^{st}\right)^2 \tag{82}$$

and B_1^{st} can be found by substituting Equation (82) into Equation (81) for $p = 1$, being

$$2\mathbb{I}(\beta_{1,b} + \beta_{1,s})B_1^{st} + (\omega_{1,b} + \omega_{1,s}) + (K(1,-1) + K(1,2))\frac{K(2,1)}{2\mathbb{I}(\beta_{2,b} + \beta_{2,s})}\left(B_1^{st}\right)^3 = 0 \tag{83}$$

The resulting values for B_1^{st} and B_2^{st} are depicted in Figure 7 over the applied stretch λ_z for two different values for the elastocapillary ratio and a given surface imperfection.

It is found that both B_1^{st} and B_2^{st} are real functions only for $\lambda_z < \bar{\lambda_z}$. This limiting value $\bar{\lambda_z}$, that depends on the choice of $\frac{L_{ec}}{R_0}$, is just beyond the stability threshold for the perfect system and it can be possibly related to the presence of a turning point, which might suggest the presence of a subcritical bifurcation, as observed in the perfect system. Moreover, the amplitude B_2^{st} is found to be much lower than the corresponding value of B_1^{st} (about 100

times), indicating that the imperfect solution is dominated by the first-order resonating term of the modal imperfection.
Accordingly, the theoretical analysis allows to predict the evolution of the beaded cylinder radius $r_{0,imp}$ as

$$r_{0,imp} = \sqrt{2\left(\frac{R_{0,imp}^2}{2\lambda_z} - \xi B_1^{st} k_{imp} R_{0,imp} u_1|_{R=R_{0,imp}} \left(e^{\mathbb{I}k_{imp}z} + e^{-\mathbb{I}k_{imp}z}\right)\right)} \tag{84}$$

where the series development of the stream function up to the first order in ξ is considered, $R_{0,imp} = R_0 + \xi^2 \frac{2\pi}{k_{imp}} \left(e^{\mathbb{I}k_{imp}z} + e^{-\mathbb{I}k_{imp}z}\right)$ and the static amplitudes B_1^{st} are depicted in Figure 7(a). Finally, such theoretical predictions are found in very good agreement with the corresponding numerical results, as depicted in Figure 8 for the two different choices of $\frac{L_{ec}}{R_0} = 5.57$ and $\frac{L_{ec}}{R_0} = 5.80$.

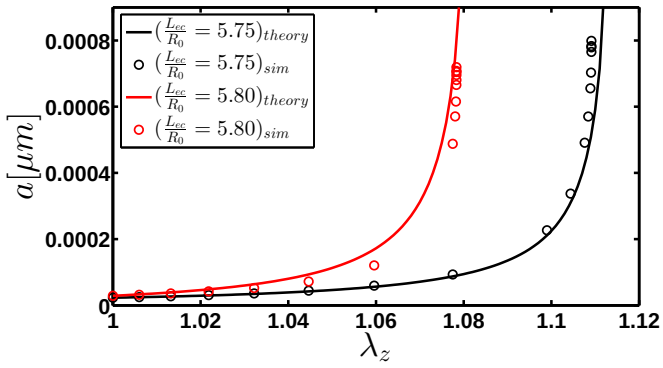

Figure 8: Comparison between the theoretical predictions (solid lines) and the numerical results (circles) for $\frac{L_{ec}}{R_0} = 5.57$ (black) and $\frac{L_{ec}}{R_0} = 5.8$ (red) in the Case (1). The two cylinders have radius $R_0 = 0.2\mu m$ and a shear modulus $\mu = 20Pa$, with the initial imperfection set to $\xi = 0.0003$ and normalized wavenumber $k_{imp} = 0.01$. The theoretical predictions and the numerical results are compared in terms of the parameter R^2: $R^2 = 0.98$ (red); $R^2 = 0.98$ (black).

8 Discussion

In this work we have investigated the onset and the non-linear development of beading in axially stretched soft cylinders with a surface tension. We have performed both a theoretical study, deriving the linear and the weakly non-linear stability analysis for the problem, and numerical simulations, investigating the fully non-linear evolution of the beaded morphology. Firstly, we have proposed an elastocapillary model in which the incompressibility constraint is enforced through the definition of a non-linear stream function in finite elasticity. Then, we have proposed a variational formulation deriving the Euler-Lagrange equations which define the boundary value problem for the soft cylinder. The problem is governed by two dimensionless parameters: the applied stretch λ_z and the elastocapillary ratio $L_{ec}/R_0 = \gamma/(\mu R_0)$.

Accordingly, the linear stability analysis has been performed by considering a small perturbation on the stream function and the resulting dispersion relations has been derived for two relevant experimental conditions, i.e. varying λ_z at fixed L_{ec}/R_0, and varying L_{ec}/R_0 for $\lambda_z = 1$.
The results of the linear stability analysis are collected in Figure 1. It is found that a large-wavelength beading can occur if the elastocapillary length L_{ec} is of the same order of magnitude of the undeformed cylinder radius R_0. In particular, we recovered the threshold value $L_{ec} = 6R_0$ if $\lambda_z = 1$, whilst we find that the presence of an axial elongation favour the onset of beading, which can occur up to a value $L_{ec}/R_0 = 4\sqrt{2} \approx 5.65$ for a limit stretch $\lambda_z^{th} = 2^{1/3} \approx 1.26$. This novel finding suggests that the axial stretch can be used in fabrication techniques to control the beading formations in soft fibres.
Secondly, we have performed a weakly non-linear analysis in order to investigate the nature of the elastocapillary bifurcation in the two cases under consideration, studying the evolution of the beading amplitude of the near-critical waves beyond the linear stability threshold. For this purpose, we have used a multiple-scale analysis in which the order parameters of the bifurcations are given in Equation (40), with the scaling arguments provided by Equation (41). After calculating the higher order solutions for the stream function, we have derived the Ginzburg-Landau equations in (69) for the beading evolution by enforcing the conservation of the total mechanical energy. The resulting pitchfork bifurcation is always found to be subcritical for very slender cylinders (i.e. $L_0 \ll R_0$), whilst it can turn supercritical for thicker cylinders, as shown in Table 1 and in B for a larger number of configurations. Moreover, the applied stretch λ_z is found to possibly control the nature of the bifurcation when considering independently the geometrical and material parameters, defined through R_0/L_0 and L_{ec}/R_0, respectively. Indeed, the weakly non-linear analysis has shown that a supercritical bifurcation is favoured for axially stretched shorter cylinders.
Thirdly, we have implemented a finite element code of the elastocapillary model to study the fully non-linear beading of the soft cylinder. The numerical code has been validated using the results of both the linear and the weakly non-linear stability analysis, showing a very good agreement with the linear stability threshold and the beading amplitude for the supercritical bifurcation, as shown in Figure 4. The fully non-linear numerical results have highlighted two different beading dynamics for the cases under consideration. In Figure 6(a), it is shown that the beading amplitude rapidly saturated at a constant value as the axial stretch is increased beyond the linear stability threshold. Conversely, the width first increases and then decreases with respect to the width of the linear stability mode. These results are of utmost importance for applications in fabrication techniques, since they demonstrate that the morphology of the beaded fibre can be completely controlled by the applied stretch. If $\lambda_z = 1$, Figure 6(b) shows that the beading amplitude monotonically grows as the elastocapillary ratio increases beyond the linear stability threshold, whilst its relative width monotonically decreases, showing the fast transition towards a bead-on-a-string morphology. Moreover, the numerical results have shown that after a first supercritical beading, the soft cylinder can undergo a secondary subcritical bifurcation, which is characterized by both a sudden jump and an hysteresis in the beading amplitude, as shown in Figure 5(b). The resulting phase diagrams for the two cases are summarized in Figure 6.

Since the bifurcation is subcritical for very slender cylinders, we have finally performed a sensitivity analysis in order to study the pattern selection in cylinders with sinusoidal surface imperfections. In this case, the modal imperfection is assumed to interact with an infinite

number of near-critical modes, with a scaling given by Equation (76), and the system of infinite Ginzburg-Landau equations in (79) has been derived. It is found that the imperfection mode resonates with the corresponding linear stability solution, therefore the sinusoidal imperfection is found to select the beading wavelength for very slender cylinders. This is in accordance with previous experimental data, showing that the emerging beaded wavelength does not scale as L_0, as predicted by the linear stability analysis for the perfect system [6, 34].

Although our work is focused on a simplified fluid-like surface energy, we highlight that the proposed variational approach allows for considering more sophisticated effects, such as diffuse interface fluid models [39] and solid behaviours, e.g. elastic material surfaces [24], elastic boundary coating with bending stiffness [45] or second-gradient effects [20].

In conclusion, we have proposed here a novel theoretical and numerical approach for studying the onset and the fully non-linear development of the elastocapillary beading in soft cylinders subjected to axial stretch. The results of this study provide important guidelines for controlling the beaded morphologies in different experimental conditions, with important applications in micro-fabrication techniques, such as electrospun fibres [21]. The morphological insights provided by the proposed approach might also be relevant for modelling some recent experimental findings in biological systems, such at the beading of stretched nerves [37] and the shape transitions observed in mithocondria during the development of neurodegenerative diseases [12, 27]. Further work will be devoted to improve the numerical code for studying the post-buckling evolution of beading after a subcritical bifurcation, developing suitable numerical methods for improving the convergence and the algorithm sensitivity to the geometrical and the material parameters.

Acknowledgements
This work was partially supported by the Start-up Packages and PhD Program project, cofunded by Regione Lombardia through the Fondo per lo sviluppo e la coesione 2007-2013 -formerly FAS and by the Progetto Giovani GNFM 2014, funded by the National Group of Mathematical Physics (GNFM-INdAM).

A Weakly non-linear stability analysis

In this Appendix, the coefficients for the higher order solutions of the unknown functions presented in Equation (44) are reported for both the Case (1) and the Case (2).

A.1 Higher order solutions for Case (1)

The second order solution of the stream function in the term $\mathbb{I}e^{2\mathbb{I}kz}\left|A\right|^2$ is given by the function g whose coefficients are calculated imposing the boundary conditions in Equation (49) into Equation (48). The coefficient α_2 reads

$$\alpha_2 = \frac{k\left(\lambda_z^3-1\right)N_{\alpha 2}}{32\lambda_z^{5/2}r_0\left(\gamma\lambda_z\left(4k^2r_0^2-1\right)+\mu r_0\left(\lambda_z^3\left(k^2r_0^2+2\right)-k^2r_0^2+4\right)\right)} \tag{85}$$

with

$$\begin{aligned} N_{\alpha 2} =& \gamma\lambda_z\left(28k^2r_0^2+\lambda_z^3\left(4k^4r_0^4+19k^2r_0^2+4\right)-7\right) \\ &+\mu r_0\left(-7k^2r_0^2+\lambda_z^6\left(k^4r_0^4-2k^2r_0^2-32\right)+\lambda_z^3\left(k^4r_0^4-3k^2r_0^2+46\right)+28\right) \end{aligned} \tag{86}$$

The coefficient β_2 is given by

$$\beta_2 = -\frac{k\sqrt{\lambda_z}\left(\lambda_z^3-1\right)N_{\beta 2}}{32r_0\left(\gamma\lambda_z\left(4k^2r_0^2-1\right)+\mu r_0\left(\lambda_z^3\left(k^2r_0^2+2\right)-k^2r_0^2+4\right)\right)} \tag{87}$$

with

$$\begin{aligned} N_{\beta 2} =& \gamma\lambda_z\left(4k^4r_0^4+6\lambda_z^3\left(7k^2r_0^2-1\right)+5k^2r_0^2+3\right) \\ &+2\mu r_0\left(3k^2\lambda_z^6r_0^2-k^2r_0^2+\lambda_z^3\left(k^4r_0^4-8k^2r_0^2+15\right)+6\right) \end{aligned} \tag{88}$$

The third order solution of the stream function in the term $e^{\mathbb{I}kz}A\left|A\right|^2$ is given by the function H, whose coefficients are calculated imposing the boundary conditions in Equation (52) into Equation (51). The coefficient α_{31} reads

$$\alpha_{31} = \frac{3k^2\lambda_z^2\left(\lambda_z^3-1\right)^2N_{\alpha 31}}{8r_0^2\left(2\left(\lambda_z^3+2\right)\mu r_0-\gamma\lambda_z\right)\left(4\gamma\lambda_z\left(k^2r_0^2-1\right)+\mu r_0\left(\lambda_z^3\left(k^2r_0^2+8\right)-k^2r_0^2+16\right)\right)} \tag{89}$$

with

$$\begin{aligned} N_{\alpha 31} =& -4\gamma^2\left(k^2\lambda_zr_0^2+\lambda_z\right)+\gamma\mu r_0\left(3\lambda_z^3\left(5k^2r_0^2+16\right)-k^2r_0^2+64\right) \\ &+4\lambda_z^2\mu^2r_0^2\left(\lambda_z^3\left(k^2r_0^2-8\right)+k^2r_0^2-112\right) \end{aligned} \tag{90}$$

The coefficient β_{31} is given by

$$\beta_{31} = \frac{3k^2\lambda_z^2\left(\lambda_z^3-1\right)^2N_{\beta 31}}{4r_0^2\left(2\left(\lambda_z^3+2\right)\mu r_0-\gamma\lambda_z\right)\left(4\gamma\lambda_z\left(k^2r_0^2-1\right)+\mu r_0\left(\lambda_z^3\left(k^2r_0^2+8\right)-k^2r_0^2+16\right)\right)} \tag{91}$$

with

$$\begin{aligned} N_{\beta 31} =& 2\gamma^2\left(k^2\lambda_zr_0^2+\lambda_z^4\right)-\gamma\mu r_0\left(\lambda_z^3\left(7k^2r_0^2+26\right)+18\lambda_z^6+12\right) \\ &+4\lambda_z^2\mu^2r_0^2\left(\lambda_z^3\left(32-k^2r_0^2\right)+4\lambda_z^6+24\right) \end{aligned} \tag{92}$$

The third order solution of the stream function in the term $e^{3\mathbb{I}kz}A^2$ is given by the function h whose coefficients are calculated imposing the boundary conditions in Equation (55) into Equation (54). The coefficient α_3 reads

$$\alpha_3 = -\frac{k^2\lambda_z^2\left(\lambda_z^3-1\right)^2N_{\alpha 3}}{24r_0^2\left(2\left(\lambda_z^3+2\right)\mu r_0-\gamma\lambda_z\right)\left(4\gamma\lambda_z\left(9k^2r_0^2-1\right)+\mu r_0\left(\lambda_z^3\left(9k^2r_0^2+8\right)-9k^2r_0^2+16\right)\right)} \tag{93}$$

with

$$\begin{aligned} N_{\alpha 3} =& -4\gamma^2\lambda_z\left(27k^2r_0^2-7\right)+\gamma\mu r_0\left(3\lambda_z^3\left(135k^2r_0^2-64\right)-27k^2r_0^2+32\right) \\ &+4\lambda_z^2\mu^2r_0^2\left(\lambda_z^3\left(27k^2r_0^2+104\right)+27k^2r_0^2-80\right) \end{aligned} \tag{94}$$

The coefficient β_3 is given by

$$\beta_3 = \frac{k^2\lambda_z^2\left(\lambda_z^3-1\right)^2N_{\beta 3}}{12r_0^2\left(2\left(\lambda_z^3+2\right)\mu r_0-\gamma\lambda_z\right)\left(4\gamma\lambda_z\left(9k^2r_0^2-1\right)+\mu r_0\left(\lambda_z^3\left(9k^2r_0^2+8\right)-9k^2r_0^2+16\right)\right)} \tag{95}$$

with

$$\begin{aligned} N_{\beta 3} =& 2\gamma^2\lambda_z\left(-27k^2r_0^2+2\lambda_z^3+5\right)+\gamma\mu r_0\left(\lambda_z^3\left(189k^2r_0^2-46\right)-30\lambda_z^6-4\right) \\ &+4\lambda_z^2\mu^2r_0^2\left(27k^2\lambda_z^3r_0^2+20\lambda_z^6-8\right) \end{aligned} \tag{96}$$

A.2 Higher order solutions for Case (2)

Similarly to the Case (1), the coefficients of the same functions are presented for the Case (2). The second order solution of the stream function in the term $\mathbb{I}e^{2\mathbb{I}kz}\left|A\right|^2$ is given by the function g whose coefficients are calculated imposing the boundary conditions in Equation (58) into Equation (57). The coefficient α_2 reads

$$\alpha_2 = \frac{3k^2 N_{\alpha 2}}{16 D_{\alpha 2}} \tag{97}$$

with

$$\begin{aligned} N_{\alpha 2} = \gamma \left(1331k^8r_0^8 + 4816k^6r_0^6 + 15600k^4r_0^4 + 17424k^2r_0^2 - 3744\right) \\ + 4\mu r_0 \left(118k^8r_0^8 + 651k^6r_0^6 + 2124k^4r_0^4 + 4536k^2r_0^2 + 6480\right) \end{aligned} \tag{98}$$

and

$$\begin{aligned} D_{\alpha 2} = \gamma \left(k^2r_0^2 \left(25k^8r_0^8 - 30k^6r_0^6 - 2148k^4r_0^4 - 6192k^2r_0^2 - 5184\right) + 1728\right) \\ - 2\mu r_0 \left(k^2r_0^2 \left(k^8r_0^8 + 54k^6r_0^6 + 684k^4r_0^4 + 2736k^2r_0^2 + 5184\right) + 5184\right) \end{aligned} \tag{99}$$

The coefficient β_2 is given by

$$\beta_2 = -\frac{18k^4 \left(3\gamma \left(61k^6r_0^6 + 117k^4r_0^4 + 166k^2r_0^2 - 12\right) + 2\mu r_0 \left(34k^6r_0^6 + 109k^4r_0^4 + 162k^2r_0^2 + 252\right)\right)}{D_{\beta 2}} \tag{100}$$

with

$$\begin{aligned} D_{\beta 2} = \gamma \left(k^2r_0^2 \left(-25k^8r_0^8 + 30k^6r_0^6 + 2148k^4r_0^4 + 6192k^2r_0^2 + 5184\right) - 1728\right) \\ + 2\mu r_0 \left(k^2r_0^2 \left(k^8r_0^8 + 54k^6r_0^6 + 684k^4r_0^4 + 2736k^2r_0^2 + 5184\right) + 5184\right) \end{aligned} \tag{101}$$

The third order solution of the stream function in the term $e^{\mathbb{I}kz}A\left|A\right|^2$ is given by the function H whose coefficients are calculated imposing the boundary conditions in Equation (61) into Equation (60). The coefficient α_{31} read

$$\alpha_{31} = -\frac{144k^4 N_{\alpha 31}}{(\gamma - 6\mu r_0) D_{\alpha 31}} \tag{102}$$

with

$$\begin{aligned} N_{\alpha 31} = 4\gamma^2 \left(25k^6r_0^6 + 324k^4r_0^4 + 576k^2r_0^2 + 2304\right) \\ - \gamma\mu r_0 \left(457k^6r_0^6 + 7632k^4r_0^4 + 51840k^2r_0^2 + 175104\right) \\ + 24\mu^2 r_0^2 \left(13k^6r_0^6 + 528k^4r_0^4 + 8832k^2r_0^2 + 27648\right) \end{aligned} \tag{103}$$

and

$$\begin{aligned} D_{\alpha 31} = \gamma \left(k^2r_0^2 \left(25k^8r_0^8 - 120k^6r_0^6 - 34368k^4r_0^4 - 396288k^2r_0^2 - 1327104\right) + 1769472\right) \\ - 2\mu r_0 \left(k^2r_0^2 \left(k^8r_0^8 + 216k^6r_0^6 + 10944k^4r_0^4 + 175104k^2r_0^2 + 1327104\right) + 5308416\right) \end{aligned} \tag{104}$$

Coefficient β_{31} is given by

$$\beta_{31} = -\frac{6912k^6 N_{\beta 31}}{(\gamma - 6\mu r_0) D_{\beta 31}} \tag{105}$$

with

$$\begin{aligned} N_{\beta 31} = {} & \gamma^2 \left(25k^4r_0^4 + 216k^2r_0^2 + 192\right) \\ & - 4\gamma\mu r_0 \left(29k^4r_0^4 + 336k^2r_0^2 + 1344\right) + 8\mu^2 r_0^2 \left(11k^4r_0^4 + 312k^2r_0^2 + 2880\right) \end{aligned} \tag{106}$$

and

$$\begin{aligned} D_{\beta 31} = {} & \gamma \left(k^2r_0^2 \left(25k^8r_0^8 - 120k^6r_0^6 - 34368k^4r_0^4 - 396288k^2r_0^2 - 1327104\right) + 1769472\right) \\ & - 2\mu r_0 \left(k^2r_0^2 \left(k^8r_0^8 + 216k^6r_0^6 + 10944k^4r_0^4 + 175104k^2r_0^2 + 1327104\right) + 5308416\right) \end{aligned} \tag{107}$$

The third order solution of the stream function in the term $e^{3\mathbb{I}kz}A^2$ is given by the function h whose coefficients are calculated imposing the boundary conditions in Equation (64) into Equation (63). Coefficient α_3 reads

$$\alpha_3 = \frac{16k^4 N_{\alpha 3}}{9(\gamma - 6\mu r_0) D_{\alpha 3}} \tag{108}$$

with

$$\begin{aligned} N_{\alpha 3} = {} & \gamma^2 \left(27k^2r_0^2 \left(795k^4r_0^4 + 896k^2r_0^2 - 384\right) - 2048\right) \\ & + 648\gamma k^4 r_0^4 \left(21k^2r_0^2 + 8\right) \left(2\log(r_0) - \log\left(r_0^2\right)\right) (2\gamma - 11\mu r_0) \\ & + \gamma\mu r_0 \left(-75897k^6r_0^6 - 72144k^4r_0^4 + 58752k^2r_0^2 + 5120\right) \\ & - 24\mu^2 r_0^2 \left(9k^2r_0^2 \left(153k^4r_0^4 + 336k^2r_0^2 + 128\right) - 1024\right) \end{aligned} \tag{109}$$

and

$$\begin{aligned} D_{\alpha 3} = {} & 648k^4r_0^4 \left(21k^2r_0^2 + 8\right) \left(2\log(r_0) - \log\left(r_0^2\right)\right) \\ & \left(\gamma \left(621k^4r_0^4 + 504k^2r_0^2 - 64\right) + 2\mu r_0 \left(27k^2r_0^2 \left(5k^2r_0^2 + 8\right) + 64\right)\right) \\ & + \gamma \left(27k^2r_0^2 \left(2025k^8r_0^8 - 1080k^6r_0^6 - 34368k^4r_0^4 - 44032k^2r_0^2 - 16384\right) + 65536\right) \\ & - 6\mu r_0 \left(9k^2r_0^2 \left(81k^8r_0^8 + 1944k^6r_0^6 + 10944k^4r_0^4 + 19456k^2r_0^2 + 16384\right) + 65536\right) \end{aligned} \tag{110}$$

The coefficient β_3 is given by

$$\beta_3 = \frac{256k^6 N_{\beta 3}}{(\gamma - 6\mu r_0) D_{\beta 3}} \tag{111}$$

with

$$\begin{aligned} N_{\beta 3} = {} & \gamma^2 \left(1755k^4r_0^4 + 1224k^2r_0^2 - 448\right) - 32\gamma\mu r_0 \left(189k^4r_0^4 + 99k^2r_0^2 - 80\right) \\ & - 24\mu^2 r_0^2 \left(27k^2r_0^2 \left(5k^2r_0^2 + 8\right) + 64\right) \end{aligned} \tag{112}$$

and

$$\begin{aligned} D_{\beta 3} = {} & 648k^4r_0^4 \left(21k^2r_0^2 + 8\right) \left(2\log(r_0) - \log\left(r_0^2\right)\right) \\ & \left(\gamma \left(621k^4r_0^4 + 504k^2r_0^2 - 64\right) + 2\mu r_0 \left(27k^2r_0^2 \left(5k^2r_0^2 + 8\right) + 64\right)\right) \\ & + \gamma \left(27k^2r_0^2 \left(2025k^8r_0^8 - 1080k^6r_0^6 - 34368k^4r_0^4 - 44032k^2r_0^2 - 16384\right) + 65536\right) \\ & - 6\mu r_0 \left(9k^2r_0^2 \left(81k^8r_0^8 + 1944k^6r_0^6 + 10944k^4r_0^4 + 19456k^2r_0^2 + 16384\right) + 65536\right) \end{aligned} \tag{113}$$

B Series expansion of the total energy

The coefficients of the energy term in Equation (68), corresponding to the fourth order expansion in ϵ of the total energy, are presented for both the Case (1) and the Case (2).

B.1 Coefficients in the term E_4 for Case (1)

For sake of completeness, a slightly different notation is used in this subsection. According to the scaling proposed in Equation (40) for Case (1), the control parameter λ_z is perturbed around the linear threshold λ_z^{th} such that $\lambda_z = \lambda_z^{th}\left(\epsilon^2 + 1\right)$. In the energy expansion there is the need of making explicit this dependence for the function u introduced in Equation (23): therefore, in this subsection, $u = u\left(r, \lambda_z\right)$ and the derivative will be presented as $u^{(l_1,l_2)}$ where the l_1 indicates the order of derivation with respect to the first argument and l_2 the derivative with respect to the second one. No change of notation is done for the other functions. The coefficient γ_v becomes

$$\gamma_v = \frac{2\pi\rho_0\left(\left(k^2R^2 + \lambda_z^{th}\right)u^2 + R^2\left(u^{(1,0)}\right)^2 + 2\sqrt{\lambda_z^{th}}Ru^{(1,0)}u\right)}{kR\tau_c^2} \tag{114}$$

Coefficient α_v can be written as

$$\alpha_v = \frac{2\pi\mu}{k\lambda_z^{th}R^5}$$
$$\left(-6k^4R^5u\left(u^{(1,0)}\right)^3\left(\lambda_z^{th}\right)^{3/2}+2k^2R^5uu^{(1,0)}\left(u^{(2,0)}\right)^2\left(\lambda_z^{th}\right)^{3/2}+8k^3R^4u^2g'\left(\lambda_z^{th}\right)^{3/2}\right.$$
$$-2R^3uH'\left(\lambda_z^{th}\right)^{3/2}+2k^2R^5\left(u^{(1,0)}\right)^3u^{(2,0)}\left(\lambda_z^{th}\right)^{3/2}-6kR^4ug'u^{(2,0)}\left(\lambda_z^{th}\right)^{3/2}$$
$$+2k^4R^5u^2u^{(1,0)}u^{(2,0)}\left(\lambda_z^{th}\right)^{3/2}+4kR^2u^2g'\left(\lambda_z^{th}\right)^{5/2}-16k^4R^3u^3u^{(1,0)}\left(\lambda_z^{th}\right)^{5/2}$$
$$-2k^2R^3u^2u^{(1,0)}u^{(2,0)}\left(\lambda_z^{th}\right)^{5/2}-6k^3R^6g'\left(u^{(1,0)}\right)^2\left(\lambda_z^{th}\right)^{7/2}+2k^5R^6u^2g'\left(\lambda_z^{th}\right)^{7/2}$$
$$+2k^2R^5uH'\left(\lambda_z^{th}\right)^{7/2}+12k^4R^5u\left(u^{(1,0)}\right)^3\left(\lambda_z^{th}\right)^{9/2}-6k^3R^4u^2g'\left(\lambda_z^{th}\right)^{9/2}$$
$$+4k^6R^5u^3u^{(1,0)}\left(\lambda_z^{th}\right)^{9/2}+12k^4R^3u^3u^{(1,0)}\left(\lambda_z^{th}\right)^{11/2}+3k^4R^2u^4\left(\lambda_z^{th}\right)^6$$
$$+7k^6R^4u^4\left(\lambda_z^{th}\right)^5+18k^4R^4u^2\left(u^{(1,0)}\right)^2\left(\lambda_z^{th}\right)^5+k^2u^4\left(\lambda_z^{th}\right)^4$$
$$+3k^4R^6\left(u^{(1,0)}\right)^4\left(\lambda_z^{th}\right)^4+k^6R^6u^2\left(u^{(1,0)}\right)^2\left(\lambda_z^{th}\right)^4-12k^3R^5ug'u^{(1,0)}\left(\lambda_z^{th}\right)^4$$
$$+5k^4R^2u^4\left(\lambda_z^{th}\right)^3+4k^2R^6g'^2\left(\lambda_z^{th}\right)^3-2k^2R^2u^2\left(u^{(1,0)}\right)^2\left(\lambda_z^{th}\right)^3$$
$$+2k^2R^6H'u^{(1,0)}\left(\lambda_z^{th}\right)^3-2k^2R^2u^3u^{(2,0)}\left(\lambda_z^{th}\right)^3+k^2R^4\left(u^{(1,0)}\right)^4\left(\lambda_z^{th}\right)^2$$
$$+17k^4R^4u^2\left(u^{(1,0)}\right)^2\left(\lambda_z^{th}\right)^2+k^2R^4u^2\left(u^{(2,0)}\right)^2\left(\lambda_z^{th}\right)^2-4kR^3ug'u^{(1,0)}\left(\lambda_z^{th}\right)^2$$
$$+2kR^3u^2g''\left(\lambda_z^{th}\right)^2-2k^4R^4u^3u^{(2,0)}\left(\lambda_z^{th}\right)^2+2k^2R^4u\left(u^{(1,0)}\right)^2u^{(2,0)}\left(\lambda_z^{th}\right)^2$$
$$+R^2\left(16k^4\left(\lambda_z^{th}\right)^2R^4+4k^2\left(\lambda_z^{th}\right)^3R^2+4k^2R^2+\lambda_z^{th}\right)g^2\lambda_z^{th}$$
$$+R^4g'^2\lambda_z^{th}+3k^4R^6u^2\left(u^{(2,0)}\right)^2\lambda_z^{th}+k^2R^6\left(u^{(1,0)}\right)^2\left(u^{(2,0)}\right)^2\lambda_z^{th}$$
$$-14k^3R^5ug'u^{(1,0)}\lambda_z^{th}+2R^4H'u^{(1,0)}\lambda_z^{th}-2k^3R^5u^2g''\lambda_z^{th}$$
$$-2kR^5\left(u^{(1,0)}\right)^2g''\lambda_z^{th}-2R^4uH''\lambda_z^{th}+2kR^5g'u^{(1,0)}u^{(2,0)}\lambda_z^{th}$$
$$-2kR^5ug''u^{(2,0)}\lambda_z^{th}+6k^3R^6g'\left(u^{(1,0)}\right)^2\sqrt{\lambda_z^{th}}+2kR^6g'\left(u^{(2,0)}\right)^2\sqrt{\lambda_z^{th}}$$
$$+4k^2R^5uH'\sqrt{\lambda_z^{th}}+2R^5g'g''\sqrt{\lambda_z^{th}}+2k^3R^6uu^{(1,0)}g''\sqrt{\lambda_z^{th}}$$
$$+2R^5u^{(1,0)}H''\sqrt{\lambda_z^{th}}-4k^3R^6ug'u^{(2,0)}\sqrt{\lambda_z^{th}}+2R^5H'u^{(2,0)}\sqrt{\lambda_z^{th}}$$
$$-2kR^6u^{(1,0)}g''u^{(2,0)}\sqrt{\lambda_z^{th}}+12k^2R^6g'^2+R^6g''^2+6k^2R^6H'u^{(1,0)}$$
$$+2k^2R^6uH''+2R^6H''u^{(2,0)}+2R^2H\left(\lambda_z^{th}\left(k^4\left(\lambda_z^{th}\right)^2R^4+k^2\left(\lambda_z^{th}\right)^3R^2+k^2R^2+\lambda_z^{th}\right)u\right.$$
$$\left.+R\left(\sqrt{\lambda_z^{th}}\left(k^2R^2\left(\lambda_z^{th}\right)^3-\lambda_z^{th}+2k^2R^2\right)u^{(1,0)}+R\left(k^2R^2-\lambda_z^{th}\right)u^{(2,0)}\right)\right)$$
$$-2R^2g\left(3k^3R\left(3k^2R^2+\lambda_z^{th}\right)u^2\left(\lambda_z^{th}\right)^4\right.$$
$$\left.+ku\left(\sqrt{\lambda_z^{th}}\left(4k^4\left(\lambda_z^{th}\right)^2R^4+6k^2\left(\lambda_z^{th}\right)^3R^2+k^2R^2+2\lambda_z^{th}\right)u^{(1,0)}+R\left(2k^2R^2+\lambda_z^{th}\right)u^{(2,0)}\right)\lambda_z^{th}\right.$$
$$\left.-R\left(k\lambda_z^{th}\left(-3k^2R^2\left(\lambda_z^{th}\right)^3+2\lambda_z^{th}+k^2R^2\right)\left(u^{(1,0)}\right)^2\right.\right.$$

The coefficient α_s reads

$$\begin{aligned}\alpha_s = &-\frac{\pi\gamma k\sqrt{\lambda_z^{th}}}{2R_0^3}\\ &\left(24k\lambda_z^{th}R_0\left(k^2R_0^2-\lambda_z^{th}\right)gu^2+16R_0^2\left(\lambda_z^{th}-4k^2R_0^2\right)g^2\right.\\ &\left.+u\left(8R_0^2\left(\lambda_z^{th}-k^2R_0^2\right)H+3k^2\lambda_z^{th}\left(k^4R_0^4-2k^2\lambda_z^{th}R_0^2+5\left(\lambda_z^{th}\right)^2\right)u^3\right)\right)\end{aligned} \tag{116}$$

The coefficient β_v is given by

$$\begin{aligned}\beta_v = &\frac{2\pi\mu}{k\lambda_z^{th}R^3}\\ &\left(R\left(2\lambda_z^{th}u^{(0,1)}\left(\sqrt{\lambda_z^{th}}\left(k^2\left(\lambda_z^{th}\right)^3R^2+2k^2R^2-\lambda_z^{th}\right)u^{(1,0)}+R\left(k^2R^2-\lambda_z^{th}\right)u^{(2,0)}\right)\right.\right.\\ &+R\left(\left(3k^2\left(\lambda_z^{th}\right)^3R^2+\lambda_z^{th}\right)\left(u^{(1,0)}\right)^2\right.\\ &+2u^{(1,0)}\left(\lambda_z^{th}\left(k^2\left(\lambda_z^{th}\right)^3R^2+3k^2R^2+\lambda_z^{th}\right)u^{(1,1)}+\sqrt{\lambda_z^{th}}R\left(u^{(2,0)}+\lambda_z^{th}u^{(2,1)}\right)\right)\\ &\left.\left.+Ru^{(2,0)}\left(2\left(\lambda_z^{th}\right)^{3/2}u^{(1,1)}+R\left(u^{(2,0)}+2\lambda_z^{th}u^{(2,1)}\right)\right)\right)\right)\\ &+\left(\lambda_z^{th}\right)^2\left(2k^4\lambda_z^{th}R^4+3k^2\left(\lambda_z^{th}\right)^2R^2+1\right)u^2\\ &+2\lambda_z^{th}u\left(R\left(\sqrt{\lambda_z^{th}}\left(k^2\left(\lambda_z^{th}\right)^3R^2+2k^2R^2-\lambda_z^{th}\right)u^{(1,1)}\right.\right.\\ &+\sqrt{\lambda_z^{th}}\left(3k^2\left(\lambda_z^{th}\right)^2R^2-1\right)u^{(1,0)}+R\left(\left(k^2R^2-\lambda_z^{th}\right)u^{(2,1)}-u^{(2,0)}\right)\Big)\\ &\left.\left.+\lambda_z^{th}\left(k^4\left(\lambda_z^{th}\right)^2R^4+k^2\left(\lambda_z^{th}\right)^3R^2+k^2R^2+\lambda_z^{th}\right)u^{(0,1)}\right)\right)\end{aligned} \tag{117}$$

Finally, the coefficient β_s reads

$$\beta_s = \frac{\pi\gamma k\sqrt{\lambda_z^{th}}u\left(\left(k^2R_0^2-3\lambda_z^{th}\right)u-4\lambda_z^{th}\left(\lambda_z^{th}-k^2R_0^2\right)u^{(0,1)}\right)}{R_0} \tag{118}$$

B.2 Coefficients in the term E_4 for Case (2)

Also for Case (2), a slightly different notation with respect to the manuscript is used in this subsection. According to the scaling proposed in Equation (40) for Case (2), the control parameter μ is perturbed around the linear threshold μ^{th} such that $\mu = \mu^{th}\left(\epsilon^2+1\right)$. In this case the explicit dependence of function u presented in Equation (23) on parameter μ should be stated: therefore, in this subsection, $u = u\left(r,\mu\right)$ and the derivative will be presented as $u^{(l_1,l_2)}$ where the l_1 indicates the order of derivation with respect to the first argument and l_2 the derivative with respect to the second one. No change of notation is done for the other functions.

The coefficient γ_v reads

$$\gamma_v = \frac{2\pi\rho_0 \left(\left(k^2R^2+1\right)u^2 + R^2\left(u^{(1,0)}\right)^2 + 2Ru^{(1,0)}u \right)}{kR\tau_c^2} \tag{119}$$

The coefficient α_v can be written as

$$\begin{aligned}
\alpha_v = & \frac{2\pi m u^{th}}{kR^5} \\
& \Bigg(7R^4u^4k^6 + R^6u^2\left(u^{(1,0)}\right)^2k^6 + 4R^5u^3u^{(1,0)}k^6 + 2R^6u^2g'k^5 \\
& +8R^2u^4k^4 + 3R^6\left(u^{(1,0)}\right)^4k^4 + 6R^5u\left(u^{(1,0)}\right)^3k^4 \\
& +35R^4u^2\left(u^{(1,0)}\right)^2k^4 + 3R^6u^2\left(u^{(2,0)}\right)^2k^4 \\
& -4R^3u^3u^{(1,0)}k^4 - 2R^4u^3u^{(2,0)}k^4 + 2R^5u^2u^{(1,0)}u^{(2,0)}k^4 \\
& +2R^4u^2g'k^3 - 26R^5ug'u^{(1,0)}k^3 - 2R^5u^2g''k^3 \\
& +2R^6uu^{(1,0)}g''k^3 - 4R^6ug'u^{(2,0)}k^3 + u^4k^2 + R^4\left(u^{(1,0)}\right)^4k^2 \\
& +16R^6g'^2k^2 - 2R^2u^2\left(u^{(1,0)}\right)^2k^2 + R^4u^2\left(u^{(2,0)}\right)^2k^2 + R^6\left(u^{(1,0)}\right)^2\left(u^{(2,0)}\right)^2k^2 \\
& +2R^5uu^{(1,0)}\left(u^{(2,0)}\right)^2k^2 + 6R^5uH'k^2 + 8R^6H'u^{(1,0)}k^2 + 2R^6uH''k^2 - 2R^2u^3u^{(2,0)}k^2 \\
& +2R^5\left(u^{(1,0)}\right)^3u^{(2,0)}k^2 + 2R^4u\left(u^{(1,0)}\right)^2u^{(2,0)}k^2 - 2R^3u^2u^{(1,0)}u^{(2,0)}k^2 + 2R^6g'\left(u^{(2,0)}\right)^2k \\
& +4R^2u^2g'k - 4R^3ug'u^{(1,0)}k + 2R^3u^2g''k - 2R^5\left(u^{(1,0)}\right)^2g''k \\
& -6R^4ug'u^{(2,0)}k + 2R^5g'u^{(1,0)}u^{(2,0)}k - 2R^5ug''u^{(2,0)}k \\
& -2R^6u^{(1,0)}g''u^{(2,0)}k + \left(4k^2R^3+R\right)^2g^2 + R^4g'^2 + R^6g''^2 - 2R^3uH' \\
& +2R^4H'u^{(1,0)} + 2R^5g'g'' - 2R^4uH'' + 2R^5u^{(1,0)}H'' + 2R^5H'u^{(2,0)} \\
& +2R^6H''u^{(2,0)} + 2R^2H\left(u\left(k^2R^2+1\right)^2 + R\left(\left(3k^2R^2-1\right)u^{(1,0)} + R\left(k^2R^2-1\right)u^{(2,0)}\right)\right) \\
& -2R^2g\left(3\left(3R^3k^5+Rk^3\right)u^2 + k\left(\left(4k^4R^4+7k^2R^2+2\right)u^{(1,0)} + R\left(2k^2R^2+1\right)u^{(2,0)}\right)u\right. \\
& +R\Bigg(2k\left(k^2R^2-1\right)\left(u^{(1,0)}\right)^2 - kR\left(4k^2R^2+3\right)u^{(2,0)}u^{(1,0)} \\
& \left.+\left(1-12k^2R^2\right)g' + R\left(\left(1-4k^2R^2\right)g'' - kR\left(u^{(2,0)}\right)^2\right)\right)\Bigg)\Bigg)
\end{aligned} \tag{120}$$

The coefficient α_s, instead, is given by

$$\begin{aligned}
\alpha_s = & \frac{\pi\gamma k}{2R_0^3} \\
& \left(-24kR_0\left(k^2R_0^2-1\right)gu^2 + 16R_0^2\left(4k^2R_0^2-1\right)g^2\right. \\
& \left.+u\left(8R_0^2\left(k^2R_0^2-1\right)H - 3k^2\left(k^4R_0^4-2k^2R_0^2+5\right)u^3\right)\right)
\end{aligned} \tag{121}$$

The coefficient β_v reads

$$\begin{aligned}\beta_v = & \frac{2\pi\mu^{th}}{kR^3} \\ & \Big(2u\Big(\mu^{th}\left(k^2R^2+1\right)^2 u^{(0,1)} \\ & +R\Big(\left(3k^2R^2-1\right)u^{(1,0)}+\mu^{th}\left(3k^2R^2-1\right)u^{(1,1)}+R\left(k^2R^2-1\right)\Big(u^{(2,0)}+\mu^{th}u^{(2,1)}\Big)\Big)\Big) \\ & +R\Big(2\mu^{th}u^{(0,1)}\Big(\left(3k^2R^2-1\right)u^{(1,0)}+R\left(k^2R^2-1\right)u^{(2,0)}\Big) \\ & +R\Big(\left(4k^2R^2+1\right)\Big(u^{(1,0)}\Big)^2+2u^{(1,0)}\Big(\Big(4k^2\mu^{th}R^2+\mu^{th}\Big)u^{(1,1)}+R\Big(u^{(2,0)}+\mu^{th}u^{(2,1)}\Big)\Big) \\ & +Ru^{(2,0)}\mu^{th}\Big(2\mu^{th}u^{(1,1)}+R\Big(u^{(2,0)}+2\mu^{th}u^{(2,1)}\Big)\Big)\Big)\Big) \\ & +\left(k^2R^2+1\right)^2u^2\Big)\end{aligned} \tag{122}$$

Finally, we have that $\beta_s = 0$.

B.3 Weakly non linear results for Case (1) and Case (2)

The weakly non-linear analysis proposed in Section 4 allows to identify the nature of bifurcation and to estimate the amplitude evolution in the nearby of the linear threshold. The Tables 2 and 3 in this Appendix present other configurations than the ones proposed in the manuscript, both for the Case (1) and the Case (2), respectively. Some of these configurations have been also evaluated numerically as shown in the plots in Sections 6 and 7.

$\frac{L_{ec}}{R_0}$	A^{st}			λ_z^{th}		
	$\bar{k}=0.01$	$\bar{k}=0.1$	$\bar{k}=0.2$	$\bar{k}=0.01$	$\bar{k}=0.1$	$\bar{k}=0.2$
6.2	-	-	2.350𝕀 (sub)	-	-	1.0156
6.1	-	-	2.033𝕀 (sub)	-	-	1.0514
6.0	-	3.039𝕀 (sub)	0.763 (super)	-	1.0208	1.0973
5.9	1.762𝕀 (sub)	1.142𝕀 (sub)	0.151 (super)	1.0372	1.0619	1.1675
5.8	0.773𝕀 (sub)	0.881𝕀 (sub)		1.0851	1.1184	
5.75	0.582𝕀 (sub)	0.637 (super)		1.1169	1.1609	
5.7	0.469𝕀 (sub)			1.1609		

Table 2: Numerical values for the solution A^{st} and the relative nature of bifurcation for the Case (1), computed from the weakly non-linear analysis for selected conditions of $\bar{k}$ and $\frac{L_{ec}}{R_0}$. These values are obtained for an undeformed radius $R_0 = 0.2\mu m$ and a shear modulus $\mu = 20Pa$

$\frac{L_0}{R_0}$	$\bar{k}$	$\left(\frac{L_{ec}}{R_0}\right)^{th}$	A^{st}
6283.19	0.001	6.00001	0.139$\mathbb{I}$ (sub)
628.32	0.01	6.0001	0.461 (super)
125.67	0.05	6.0151	5.696 (super)
62.83	0.10	6.0606	2.903 (super)
41.88	0.15	6.1381	2.002 (super)
28.56	0.22	6.3052	1.451 (super)
20.94	0.30	6.5934	1.123 (super)
12.08	0.52	8.2277	0.381 (super)

Table 3: Numerical values for the static solution A^{st} and the relative nature of bifurcation for the Case (2) computed from the weakly non-linear analysis for selected conditions of $\bar{k}$. The ratio $\frac{L_0}{R_0}$, assuming the lowest mode $m = 1$, is also shown to be used as control parameter to discriminate the turning point between subcritcality and supercriticality. These values are obtained imposing $\gamma = 36.5mN/m$ and $R_0 = 0.24mm$ consistently with the experimental condition shown in Mora et al. [35].

C Imperfection sensitivity analysis: coefficients of the energy series expansion

In this Appendix, we show the expression of the coefficient presented in Equation (77), describing the series expansion up to the third order in ξ of the total energy used for the imperfection sensitivity analysis in Section 7. At the zeroth order, the bulk and the superficial contributions can be written, respectively, as

$$E_{b0} = \frac{\pi\left(\left(\lambda_z^{th}\right)^3 - 3\lambda_z^{th} + 2\right)\mu R_0^2}{2k_{imp}\left(\lambda_z^{th}\right)^2} \tag{123}$$

and

$$E_{s0} = \frac{2\pi\gamma R_0}{\sqrt{\lambda_z^{th}}k_{imp}} \tag{124}$$

At the first order in ξ, the bulk and the superficial contributions can be written, respectively, as

$$E_{b1} = -\alpha_{imp}\frac{\pi\left(\left(\lambda_z^{th}\right)^3 + 3\lambda_z^{th} - 4\right)\mu R_0^2}{2k_{imp}\left(\lambda_z^{th}\right)^2} \tag{125}$$

$$E_{s1} = \alpha_{imp}\frac{\pi\gamma R_0}{\sqrt{\lambda_z^{th}}k_{imp}} \tag{126}$$

At the second order in ξ, the bulk and the superficial contributions can be written, respectively, as

$$E_{b2} = -\alpha_{imp}^2\frac{3\pi(\lambda_z^{th} - 2)\mu R_0^2}{2k_{imp}\left(\lambda_z^{th}\right)^2} \tag{127}$$

$$E_{s2} = \alpha_{imp}^2\frac{3\pi\gamma R_0}{4k_{imp}\sqrt{\lambda_z^{th}}} \tag{128}$$

At the third order in ξ, the coefficients are presented as show in Equation (77). The bulk and superficial contributions that multiply the term $\left|\frac{\partial A_n(\tau)}{\partial \tau}\right|^2$ are given by

$$\nu_{n,b} = \frac{2\alpha_{imp}\rho_0\pi}{k_{imp}\tau_c^2}\int_0^{R_0}\left(\frac{1}{R}\left(\lambda_z^{th} + k_{imp^2}n^2R^2U_n^2 + 2\sqrt{\lambda_z^{th}}RU_nU_n^{(1,0)} + R^2\left(U_n^{(1,0)}\right)^2\right)\right)dR \tag{129}$$

$$\nu_{n,s} = 0 \tag{130}$$

The bulk and superficial contributions that multiply the term $\left(|A_n(\tau)|\right)^2$ are

$$\begin{aligned}
\beta_{n,b} = &-\frac{\pi 2\mu}{k_{imp}\lambda_z^{th}R^3} \\
&\left(R\left(2\lambda_z^{th}U_n^{(0,1)}\left(\sqrt{\lambda_z^{th}}\left(k_{imp}^2\left(\lambda_z^{th}\right)^3n^2R^2 + 2k_{imp}^2n^2R^2 - \lambda_z^{th}\right)U_n^{(1,0)} + R\left(k_{imp}^2n^2R^2 - \lambda_z^{th}\right)U_n^{(2,0)}\right)\right.\right. \\
&+R\left(\left(3k_{imp}^2\left(\lambda_z^{th}\right)^3n^2R^2 + \lambda_z^{th}\right)\left(U_n^{(1,0)}\right)^2\right. \\
&+2U_n^{(1,0)}\left(\lambda_z^{th}\left(k_{imp}^2\left(\lambda_z^{th}\right)^3n^2R^2 + 3k_{imp}^2n^2R^2 + \lambda_z^{th}\right)U_n^{(1,1)} + \sqrt{\lambda_z^{th}}R\left(U_n^{(2,0)} + \lambda_z^{th}U_n^{(2,1)}\right)\right) \\
&\left.\left.\left.+RU_n^{(2,0)}\left(2\left(\lambda_z^{th}\right)^{3/2}U_n^{(1,1)} + R\left(U_n^{(2,0)} + 2\lambda_z^{th}U_n^{(2,1)}\right)\right)\right)\right) \\
&+\left(\lambda_z^{th}\right)^2\left(2k_{imp}^4\lambda_z^{th}n^4R^4 + 3k_{imp}^2\left(\lambda_z^{th}\right)^2n^2R^2 + 1\right)U_n^2 \\
&+2\lambda_z^{th}U_n\left(R\left(\sqrt{\lambda_z^{th}}\left(k_{imp}^2\left(\lambda_z^{th}\right)^3n^2R^2 + 2k_{imp}^2n^2R^2 - \lambda_z^{th}\right)U_n^{(1,1)}\right.\right. \\
&+\sqrt{\lambda_z^{th}}\left(3k_{imp}^2\left(\lambda_z^{th}\right)^2n^2R^2 - 1\right)U_n^{(1,0)} + R\left(\left(k_{imp}^2n^2R^2 - \lambda_z^{th}\right)U_n^{(2,1)} - U_n^{(2,0)}\right)\Big) \\
&\left.\left.+\lambda_z^{th}\left(k_{imp}^4\left(\lambda_z^{th}\right)^2n^4R^4 + k_{imp}^2\left(\lambda_z^{th}\right)^3n^2R^2 + k_{imp}^2n^2R^2 + \lambda_z^{th}\right)U_n^{(0,1)}\right)\right)
\end{aligned} \tag{131}$$

and

$$\beta_{n,s} = \begin{cases} \frac{\pi\gamma k_{imp}\sqrt{\lambda_z^{th}}n^2U_n\left(\lambda_z^{th}\left(k_{imp}^2n^2\left(4-4n^2\right)R_0^2+\lambda_z^{th}\left(4n^2-4\right)\right)U_n^{(0,1)}+\left(k_{imp}^2n^2\left(1-n^2\right)R_0^2+\lambda_z^{th}\left(3n^2-3\right)\right)U_n\right)}{(n^2-1)R_0} & \text{if } n \neq 1 \\ \frac{\pi\gamma k_{imp}\sqrt{\lambda_z^{th}}U_1\left(\lambda_z^{th}\left(4\lambda_z^{th}-4k_{imp}^2R_0^2\right)U_1^{(0,1)}+\left(3\lambda_z^{th}-k_{imp}^2R_0^2\right)U_1\right)}{R_0} & \text{if } n = 1 \end{cases} \tag{132}$$

The bulk and superficial contributions that multiply the term $\left(A_1(\tau) - A_{-1}(\tau)\right)$ are given by

$$\omega_{1,b} = -\frac{2\mathbb{I}\pi^2\left(\left(\lambda_z^{th}\right)^3 + 3\lambda_z^{th} - 4\right)\mu\left(R_0U_1^{(1,0)} + \sqrt{\lambda_z^{th}}U_1\right)}{k_{imp}\left(\lambda_z^{th}\right)^{3/2}} \tag{133}$$

$$\omega_{1,s} = \frac{4\pi^2\mathbb{I}\gamma U_1^{(1,0)}}{k_{imp}} \tag{134}$$

Coefficient B, in which the bulk and superficial contribution are condensed, is written as

$$B = \alpha_{imp}^3 \frac{\left(3 - \frac{8}{\lambda_z^{th}}\right)(\pi\mu R_0^2)}{2k_{imp}\lambda_z^{th}} - \frac{5\pi\gamma R_0}{8k_{imp}\lambda_z^{th}} \tag{135}$$

The coefficients that multiply the term $A_m(\tau)\,A_{n-m}(\tau)\,A_{-n}(\tau)$ are

$$
\begin{aligned}
Q(m,n) = {} & \frac{2\mathbb{I}\pi\mu}{\sqrt{\lambda_z^{th}}}\int_0^{R_0}\frac{1}{R^3}\\
& \Big(U_m\Big(\sqrt{\lambda_{z,th}}nU_{n-m}\Big(\sqrt{\lambda_{z,th}}\Big(k_{imp}^4\left(\lambda_{z,th}\right)^2m^2(m-n)^2R^4\\
& +k_{imp}^2n^2R^2+3k_{imp}^2\left(\lambda_{z,th}\right)^3m(m-n)R^2+2\lambda_{z,th}\Big)U_{-n}^{(1,0)}\\
& +R\left(k_{imp}^2m(m-n)R^2+\lambda_{z,th}\right)U_{-n}^{(2,0)}\Big)\\
& +\sqrt{\lambda_{z,th}}(m-n)U_{-n}\Big(3k_{imp}^2mnR\left(k_{imp}^2\left(m^2-nm+n^2\right)R^2+\lambda_{z,th}\right)U_{n-m}\left(\lambda_{z,th}\right)^3\\
& +\Big(k_{imp}^4\left(\lambda_{z,th}\right)^2m^2n^2R^4+k_{imp}^2(m-n)^2R^2+3k_{imp}^2\left(\lambda_{z,th}\right)^3mnR^2+2\lambda_{z,th}\Big)U_{n-m}^{(1,0)}\sqrt{\lambda_{z,th}}\\
& +R\left(k_{imp}^2mnR^2+\lambda_{z,th}\right)U_{n-m}^{(2,0)}\Big)\\
& -R\Big(RU_{-n}^{(2,0)}\Big(\left(k_{imp}^2m^2(m-n)R^2+\lambda_{z,th}(2m-n)\right)U_{n-m}^{(1,0)}+\sqrt{\lambda_{z,th}}mRU_{n-m}^{(2,0)}\Big)\\
& +U_{-n}^{(1,0)}\Big(\sqrt{\lambda_{z,th}}m\Big(3k_{imp}^2n(n-m)R^2\left(\lambda_{z,th}\right)^3+2\lambda_{z,th}+k_{imp}^2\left(m^2-3nm+3n^2\right)R^2\Big)U_{n-m}^{(1,0)}\\
& +R\left(k_{imp}^2m^2nR^2+\lambda_{z,th}(m+n)\right)U_{n-m}(2,0)\Big)\Big)\Big)\\
& +U_{-n}\Big(\sqrt{\lambda_{z,th}}mU_{n-m}\Big(\sqrt{\lambda_{z,th}}\Big(-k_{imp}^4\left(\lambda_{z,th}\right)^2(m-n)^2n^2R^4\\
& -k_{imp}^2m^2R^2+3k_{imp}^2\left(\lambda_{z,th}\right)^3(m-n)nR^2-2\lambda_{z,th}\Big)U_m^{(1,0)}\\
& +R\left(k_{imp}^2(m-n)nR^2-\lambda_{z,th}\right)U_m^{(2,0)}\Big)\\
& +R\Big(RU_m^{(2,0)}\Big(\left(k_{imp}^2n^2(n-m)R^2-\lambda_{z,th}(m-2n)\right)U_{n-m}^{(1,0)}+\sqrt{\lambda_{z,th}}nRU_{n-m}^{(2,0)}\Big)\\
& +U_m^{(1,0)}\Big(\sqrt{\lambda_{z,th}}n\Big(3k_{imp}^2m(m-n)R^2\left(\lambda_z^{th}\right)^3+2\lambda_z^{th}+k_{imp}^2\left(3m^2-3nm+n^2\right)R^2\Big)U_{n-m}^{(1,0)}\\
& +R\Big(k_{imp}^2mn^2R^2+\lambda_z^{th}(m+n)\Big)U_{n-m}^{(2,0)}\Big)\Big)\Big)\\
& +R\Big(\Big(U_m^{(1,0)}\Big((m-n)U_{-n}^{(1,0)}\Big(3k_{imp}^2\Big(\left(\lambda_z^{th}\right)^3-1\Big)mnRU_{n-m}^{(1,0)}-\sqrt{\lambda_z^{th}}U_{n-m}^{(2,0)}\Big)\\
& -U_{-n}^{(2,0)}\Big(\sqrt{\lambda_z^{th}}nU_{n-m}^{(1,0)}+mRU_{n-m}^{(2,0)}\Big)\Big)\\
& +U_m^{(2,0)}\Big((m-n)RU_{n-m}^{(1,0)}U_{-n}^{(2,0)}+U_{-n}^{(1,0)}\Big(\sqrt{\lambda_z^{th}}mU_{n-m}^{(1,0)}+nRU_{n-m}^{(2,0)}\Big)\Big)\Big)R^2\\
& +U_{n-m}\Big(U_m^{(1,0)}\Big(\sqrt{\mathrm{lz0}}(m-n)\Big(3k_{imp}^2mnR^2\left(\mathrm{lz0}\right)^3+2\mathrm{lz0}+k_{imp}^2\left(m^2+nm+n^2\right)R^2\Big)U_{-n}^{(1,0)}\\
& +R\left(k_imp^2m(m-n)^2R^2+\mathrm{lz0}(2m-n)\right)U_{-n}^{(2,0)}\Big)\\
& -RU_m^{(2,0)}\Big(\Big(k_{imp}^2(m-n)^2nR^2-\lambda_z^{th}(m-2n)\Big)U_{-n}^{(1,0)}+\sqrt{\mathrm{lz0}}(n-m)RU_{-n}^{(2,0)}\Big)\Big)\Big)\Big)\,dR
\end{aligned}
\tag{136}
$$

$$Q_s\left(m,n\right)=\frac{2\mathbb{I}\pi\gamma k_{imp}^2\left(\lambda_z^{th}\right)^{3/2}mn(m-n)U_mU_{-n}\left(k_{imp}^2R_0^2\left(m^2-mn+n^2\right)-3\lambda_z^{th}\right)U_{n-m}}{R_0^2} \tag{137}$$

References

[1] M. Abramowitz and I.A. Stegun. *Handbook of Mathematical Functions with Formulas, Graphs, and Mathematical Tables*. Dover, New York, 1965.

[2] A. Antkowiak, B. Audoly, C. Josserand, S. Neukirch, and M. Rivetti. Instant fabrication and selection of folded structures using drop impact. *PNAS*, 108:10400–10404, 2011.

[3] R.J. Asaro and W.A. Tiller. Interface morphology development during stress corrosion cracking: Part i. via surface diffusion. *Metall. Trans.*, 3(7):1789–1796, 1972.

[4] B. Barrière, K. Sekimoto, and L. Leibler. Peristaltic instability of cylindrical gels. *J. Chem. Phys.*, 105(4):1735–1738, 1996.

[5] M.A. Biot. Surface instability of rubber in compression. *Appl. Sci. Res. A*, 12(2):168–182, 1963.

[6] Arezki Boudaoud and Sahraoui Chaïeb. Mechanical phase diagram of shrinking cylindrical gels. *Phys. Rev. E*, 68:021801, 2003.

[7] F. Brau, H. Vandeparre, A. Sabbah, C. Poulard, A. Boudaoud, and P. Damman. Multiple-length-scale elastic instability mimics parametric resonance of nonlinear oscillators. *Nat. Phys.*, 7:56–60, 2011.

[8] Zongxi Cai and Yibin Fu. Exact and asymptotic stability analyses of a coated elastic half-space. *Int. J. Solids Struct.*, 37(22):3101 – 3119, 2000.

[9] Y. Cao and J. W. Hutchinson. Wrinkling phenomena in neo-hookean film/substrate bilayers. *J. Appl. Mech.*, 79:031019, 2012.

[10] Yanping Cao and John W. Hutchinson. From wrinkles to creases in elastomers: the instability and imperfection-sensitivity of wrinkling. *Proc. R. Soc. A*, 468(2137):94–115, 2012.

[11] M.M. Carroll. A representation theorem for volume-preserving transformations. *Int. J. Nonlinear Mech.*, 39(2):219 – 224, 2004.

[12] Hsiuchen Chen and David C. Chan. Mitochondrial dynamicsfusion, fission, movement, and mitophagyin neurodegenerative diseases. *Hum. Mol. Gen.*, 18(R2):R169–R176, 2009.

[13] W.M. Choi, J. Song, D.-Y. Khang, H. Jiang, Y.Y. Huang, and J.A. Rogers. Biaxially stretchable "wavy" silicon nanomembranes. *Nano Lett.*, 7(6):1655–1663, 2007.

[14] P. Ciarletta. Generating functions for volume-preserving transformations. *Int. J. Nonlinear Mech.*, 46(9):1275 – 1279, 2011.

[15] P Ciarletta. Buckling instability in growing tumor spheroids. *Phys. Rev. Lett.*, 110(15):158102, 2013.

[16] P. Ciarletta. Wrinkle-to-fold transition in soft layers under equi-biaxial strain: A weakly nonlinear analysis. *J. Mech. Phys. Solids*, 73(0):118 – 133, 2014.

[17] P. Ciarletta and M. Ben Amar. Growth instabilities and folding in tubular organs: A variational method in non-linear elasticity. *Int. J. Nonlinear Mech.*, 47(2):248 – 257, 2012.

[18] P. Ciarletta and M. Ben Amar. Pattern formation in fiber-reinforced tubular tissues: Folding and segmentation during epithelial growth. *J. Mech. Phys. Solids*, 60(3):525 – 537, 2012.

[19] P Ciarletta, V Balbi, and E Kuhl. Pattern selection in growing tubular tissues. *Phys. Rev. Lett.*, 113(24):248101, 2014.

[20] A. Danescu and F. Sidoroff. Second gradient vs. surface energy in the asaro-grinfeld instability. *J. Phys. IV France 08*, Pr8:79 – 86, 1998.

[21] Chun I. Fong, H. and D.H. Reneker. Beaded nanofibers formed during electrospinning. *Polymer*, 40(16):4585 – 4592, 1999.

[22] Y. Fu and G.A. Rogerson. A nonlinear analysis of instability of a pre-stressed incompressible elastic plate. *Proc. Math. Phys. Sci.*, 446(1927):233–254, 1994.

[23] M.A. Grinfeld. The stress driven instability in elastic crystals: Mathematical models and physical manifestations. *J. Nonlinear Sci.*, 3(1):35–83, 1993.

[24] M.E. Gurtin and A.I. Murdoch. A continuum theory of elastic material surfaces. *Arch. Rational Mech. Anal.*, 57(4):291–323, 1975.

[25] Evan Hohlfeld and L. Mahadevan. Unfolding the sulcus. *Phys. Rev. Lett.*, 106:105702, 2011.

[26] J.W. Hutchinson. The role on nonlinear substrate elasticity in the wrinkling of thin films. *Phil. Trans. R. Soc. A*, 371:20120422, 2013.

[27] Robert E Jensen. Control of mitochondrial shape. *Curr. Opin. Cell Biol.*, 17(4):384 – 388, 2005.

[28] J.B. Kim, P. Kim, N.C. Pegard, S.J. Oh, C.R. Kagan, J.W. Fleischer, H.A. Stone, and Y.L. Loo. Wrinkles and deep folds as photonic structures in photovoltaics. *Nat. Photon.*, 6(5):327–332, 2012.

[29] K. Krieger. Extreme mechanics: Buckling down. *Nature*, 488:146–147, 2012.

[30] B. Li, Y.P. Cao, X.Q. Feng, and H. Gao. Mechanics of morphological instabilities and surface wrinkling in soft materials: a review. *Soft Matter*, 8:5728–5745, 2012.

[31] A. Logg, K.A. Mardal, and G.N. Wells. *Automated Solution of Differential Equations by the Finite Element Method*. Springer, 2012.

[32] J.E. Marsden and T.J.R. Hughes. *Mathematical Foundations of Elasticity*. Dover Civil and Mechanical Engineering Series. Dover, 1994.

[33] C. Mathon and A. Limam. Experimental collapse of thin cylindrical shells submitted to internal pressure and pure bending. *Thin Wall. Struct.*, 44(1):39 – 50, 2006.

[34] F.S. Matsuo and T. Tanaka. Patterns in shrinking gels. *Nature*, 358:482–485, 1992.

[35] Serge Mora, Ty Phou, Jean-Marc Fromental, Len M. Pismen, and Yves Pomeau. Capillarity driven instability of a soft solid. *Phys. Rev. Lett.*, 105:214301, 2010.

[36] M. Naraghi, I. Chasiotis, H. Kahn, Y. Wen, and Y. Dzenis. Mechanical deformation and failure of electrospun polyacrylonitrile nanofibers as a function of strain rate. *Appl. Phys. Lett.*, 91(15), 2007.

[37] S. Ochs, R. Pourmand, R.A. Jersild Jr, and R.N. Friedman. The origin and nature of beading: A reversible transformation of the shape of nerve fibers. *Prog. Neurobiol.*, 52(5):391 – 426, 1997.

[38] R.W. Ogden. *Non-linear Elastic Deformations*. Dover Civil and Mechanical Engineering Series. Dover Publications, 1997.

[39] A. Onuki. Second gradient vs. surface energy in the asaro-grinfeld instability. *J. Phys. Soc. Japan*, 57:703–706, 1988.

[40] Lord Rayleigh. On the instability of jets. *Proc. London Math. Soc.*, 1:4–13, 1878.

[41] R. Sattler, C. Wagner, and J. Eggers. Blistering pattern and formation of nanofibers in capillary thinning of polymer solutions. *Phys. Rev. Lett.*, 100:164502, 2008.

[42] F. Savart. Memoires sur l constitution des veines liquides lancees par des orifices circulaires en mince paroi. *Ann. Chim. Phys.*, 53, (plates in Vol. 54.):337–386, 1883.

[43] M. Shibayama and T. Tanaka. Volume phase transition and related phenomena of polymer gels. In K. Duek, editor, *Responsive Gels: Volume Transitions I*, volume 109 of *Advances in Polymer Science*, pages 1–62. Springer Berlin Heidelberg, 1993.

[44] S. Singamaneni, M.E. McConney, and V.V. Tsukruk. Swelling-induced folding in confined nanoscale responsive polymer gels. *ACS Nano*, 4(4):2327–2337, 2010.

[45] D. J. Steigmann and R. W. Ogden. Elastic surface-substrate interactions. *Proc. R. Soc. A*, 455(1982):437 – 474, 1999.

[46] T. Tallinen, J. Biggins, and L. Mahadevan. Surface sulci in squeezed soft solids. *Phys. Rev. Lett.*, 110:024302, 2013.

[47] H. Vaughan. Axisymmetric and asymmetric instabilities in elastic solid cylinders under finite axial strain. *Z. Angew. Math. Phys.*, 22(5):865–875, 1971.

[48] E.W. Wilkes. On the stability of a circular tube under end thrust. *Quart. J. Mech. Appl. Math.*, 8:88 – 100, 1955.

MOX Technical Reports, last issues

Dipartimento di Matematica
Politecnico di Milano, Via Bonardi 9 - 20133 Milano (Italy)

25/2015 Del Pra, M.; Fumagalli, A.; Scotti, A.
Well posedness of fully coupled fracture/bulk Darcy flow with XFEM

26/2015 Tagliabue, A.; Dede', L.; Quarteroni, A.
Nitsche's Method for Parabolic Partial Differential Equations with Mixed Time Varying Boundary Conditions

27/2015 Marron, J.S.; Ramsay, J.O.; Sangalli, L.M.; Srivastava, A.
Functional Data Analysis of Amplitude and Phase Variation

24/2015 Bonaventura, L:
Local Exponential Methods: a domain decomposition approach to exponential time integration of PDE.

23/2015 Paolucci, R.; Mazzieri, I.; Smerzini, C.
Anatomy of strong ground motion: near-source records and 3D physics-based numerical simulations of the Mw 6.0 May 29 2012 Po Plain earthquake, Italy

22/2015 Bonaventura, L.; Ferretti, R.
Flux form Semi-Lagrangian methods for parabolic problems

21/2015 Arena, M.; Azzone, G.; Secchi, P.; Vantini, S.
Reputational risk and corporate finance: A multi-event model

20/2015 Antonietti, P.F.; Formaggia, L.; Scotti, A.; Verani, M.; Verzotti, N.
Mimetic finite difference approximation of flows in fractured porous media

19/2015 Palamara, S.; Lange, M.; Vergara, C.; Lassila, T.; Frangi, A.F.; Quarteroni, A.
A coupled 3D-1D numerical monodomain solver for cardiac electrical activation in the myocardium with detailed Purkinje network

17/2015 Nestola, M.G.C.; Faggiano, E.; Vergara, C.; Lancellotti, R.M.; Ippolito, S,; Filippi, S.; Quartero
Computational comparison of aortic root stresses in presence of stentless and stented aortic valve bio-prostheses